

The Velocity Field Olympics: Assessing velocity field reconstructions with direct distance tracers

Richard Stiskalek,^{1,2*} Harry Desmond,³ Julien Devriendt,¹ Adrienne Slyz,¹
 Guilhem Lavaux,⁴ Michael J. Hudson,^{5,6,7} Deaglan J. Bartlett,⁴ H el ene Courtois⁸

¹*Astrophysics, University of Oxford, Denys Wilkinson Building, Keble Road, Oxford, OX1 3RH, UK*

²*Center for Computational Astrophysics, Flatiron Institute, 162 5th Ave, New York, NY 10010, USA*

³*Institute of Cosmology & Gravitation, University of Portsmouth, Dennis Sciama Building, Portsmouth, PO1 3FX, UK*

⁴*CNRS & Sorbonne Universit e, Institut d’Astrophysique de Paris (IAP), UMR 7095, 98 bis bd Arago, F-75014 Paris, France*

⁵*Waterloo Centre for Astrophysics, University of Waterloo, Waterloo, ON N2L 3G1, Canada*

⁶*Department of Physics and Astronomy, University of Waterloo, Waterloo, ON N2L 3G1, Canada*

⁷*Perimeter Institute for Theoretical Physics, Waterloo, ON N2L 2Y5, Canada*

⁸*Universit e Claude Bernard Lyon 1, IUF, IP2I Lyon, 69622 Villeurbanne, France*

Accepted XXX. Received YYY; in original form ZZZ

ABSTRACT

The peculiar velocity field of the local Universe provides direct insights into its matter distribution and the underlying theory of gravity, and is essential in cosmological analyses for modelling deviations from the Hubble flow. Numerous methods have been developed to reconstruct the density and velocity fields at $z \lesssim 0.05$, typically constrained by redshift-space galaxy positions or by direct distance tracers such as the Tully–Fisher relation, the fundamental plane, or Type Ia supernovae. We introduce a validation framework to evaluate the accuracy of these reconstructions against catalogues of direct distance tracers. Our framework assesses the goodness-of-fit of each reconstruction using Bayesian evidence, residual redshift discrepancies, velocity scaling, and the need for external bulk flows. Applying this framework to a suite of reconstructions—including those derived from the *Bayesian Origin Reconstruction from Galaxies* (BORG) algorithm and from linear theory—we find that the non-linear BORG reconstruction consistently outperforms others. We highlight the utility of such a comparative approach for supernova or gravitational wave cosmological studies, where selecting an optimal peculiar velocity model is essential. Additionally, we present calibrated bulk flow curves predicted by the reconstructions and perform a density–velocity cross-correlation using a linear theory reconstruction to constrain the growth factor, yielding $S_8 = 0.69 \pm 0.034$. This result is in significant tension with Planck but agrees with other peculiar velocity studies.

Key words: large-scale structure of the universe – galaxies: distances and redshifts – cosmology: distance scale

1 INTRODUCTION

Spectroscopic analysis of the sky, particularly of galaxies, provides fundamental insights into the nature of our Universe. The spectroscopic data is primarily encoded in redshift measurements, which combine two key components: the uniform cosmic expansion and the peculiar motions of galaxies relative to this expansion. These motions can be characterized by the first-order moment of the phase-space distribution, known as the peculiar velocity field.

The peculiar velocity field, representing the time-integrated acceleration of galaxies since their formation, serves as a powerful probe of gravitational dynamics. It plays a crucial role in validating cosmological models by enabling direct comparisons between observed galactic motions and theoretical predictions based on the dark matter distribution (Yahil et al. 1991; Pike & Hudson 2005; Davis et al. 2011; Carrick et al. 2015; Adams & Blake 2017; Dupuy et al. 2019). Furthermore, this field provides valuable insights into structure formation processes and helps constrain fundamental cosmological parameters (Nusser 2017; Huterer et al.

* richard.stiskalek@physics.ox.ac.uk

2017; Boruah et al. 2020; Adams & Blake 2020; Said et al. 2020).

The importance of peculiar velocity fields extends to major contemporary astronomical initiatives. Programmes such as SHOES (Riess et al. 2011, 2022) and LIGO–Virgo–KAGRA (Abbott et al. 2018, 2021) incorporate these measurements to account for peculiar velocities in their determinations of the Hubble constant. The peculiar velocities for the former were derived by Peterson et al. (2022); Carr et al. (2022), primarily based on the reconstruction by Carrick et al. 2015, whereas the latter relies on compilations of peculiar velocities, such as GLADE+ (Dálya et al. 2022), which are based on Jasche & Lavaux 2019. This application is particularly relevant in the context of current cosmological tensions, as peculiar velocity measurements can shed light on the S_8 tension through their relationship with the growth rate parameter $f\sigma_8 \sim S_8$ (Heymans et al. 2021; Abbott et al. 2022; Amon et al. 2022; Madhavacheril et al. 2024).

Various methodologies have been developed to reconstruct the velocity field, utilizing either redshift-space galaxy positions or direct peculiar velocity measurements. However, these reconstructions must carefully account for selection effects to avoid systematic biases. These methodological challenges, particularly in the context of comparing density and peculiar velocity fields of nearby galaxies, have been extensively analysed in the literature (Strauss & Willick 1995).

Several previous works have developed increasingly complex frameworks to compare velocity models to distance data fairly (Boruah et al. 2020; Said et al. 2020). In this work, we introduce a self-consistent framework to assess the accuracy of current reconstruction models available in the scientific literature. We account for the homogeneous and inhomogeneous Malmquist biases (Strauss & Willick 1995), distance tracer selection effects, and joint inference of standardization parameters. We apply this framework to a variety of existing models from the literature and data pairs. This includes the *Constrained Simulations in BORG* (CSiBORG) models based on the *Bayesian Origin Reconstruction from Galaxies* algorithm (BORG, e.g. Jasche & Lavaux 2019), along with other models from the literature (Carrick et al. 2015; Sorce 2018, 2020; Lilow et al. 2024). We aim to determine which models and methods are most consistent with distance data and to understand the systematic biases in each model. This should serve as a guideline for future studies that aim to use peculiar velocity data to constrain cosmological parameters and help them choose the best model for their analysis.

The article is structured as follows. In Section 2, we describe the peculiar velocity field models derived from reconstructions and distance data used in this work. In Section 3, we introduce our statistical and validation framework. In Section 4, we present the results of our analysis, which include the comparison of the evidence for the different velocity models and consistency parameters with cosmology. In Section 5, we discuss the implications of our findings. Finally, in Section 6, we summarize our conclusions. We note that all logarithms in this work are base-10, unless explicitly stated. We use the notation $\mathcal{N}(x; \mu, \sigma)$ to denote the normal distribution with mean μ and standard deviation σ evaluated at x .

2 DATA

In this section, we discuss first the different kinds of velocity model reconstructions we use in this work (Section 2.1), and then the distance data we use to validate these models (Section 2.2).

2.1 Local Universe reconstructions

We use several reconstructions of the local Universe, constrained by either redshift-space galaxy positions or peculiar velocities. The former approach typically employs a counter-voxel likelihood and requires a galaxy bias to predict the number of galaxies in a cell based on the cell’s matter density, after which it is limited mainly by shot noise. The latter relies on a (Gaussian) likelihood defined in the projected peculiar velocity, but is limited by the large noise in peculiar velocity measurements. We summarise these reconstructions in Table 1, and describe them one-by-one here.

2.1.1 Carrick et al.

In Carrick et al. (2015, hereafter C15), the luminosity-weighted density field is derived from the redshift-space positions of galaxies in the 2M++ catalogue, using the iterative scheme of Yahil et al. (1991). 2M++ is a whole-sky redshift compilation of 69,160 galaxies (Lavaux & Hudson 2011), derived from photometry from the Two-Micron-All-Sky Extended Source Catalog (Skrutskie et al. 2006) and redshifts from the 2MASS Redshifts Survey (2MRS, Huchra et al. 2012), the 6dF Galaxy Redshift Survey (Jones et al. 2009), and the Sloan Digital Sky Survey (SDSS) Data Release 7 (Abazajian et al. 2009). The 2M++ K -band apparent magnitudes are corrected for Galactic extinction, k -corrections, evolution, and surface brightness dimming. The catalogue is apparent magnitude limited to $K < 11.5$ in the regions of sky covered by 2MRS and to $K < 12.5$ within the areas covered by 6dF and SDSS.

C15 first fits a luminosity function to the 2M++ catalogue to assign luminosity weights to each galaxy. Then, the luminosity-dependent bias of Westover (2007) is applied to normalise the density contrast across all radii. Galaxy positions are moved from the redshift-space to real-space using an iterative approach. Within the inner region of ~ 125 Mpc/ h the Zone of Avoidance is masked in the 2M++ data and filled by “cloning” galaxies above and below the Galactic plane to reconstruct the density field in this region. The resulting velocity field is calculated from the density field assuming linear perturbation theory. The velocity field is independent of the dimensionless growth factor, and thus must be scaled to match the peculiar velocities (with a factor β^* in the notation of C15). This single field is generated on a 256^3 grid with a box size of $400h^{-1}$ Mpc, a voxel size of $1.6h^{-1}$ Mpc, and assuming $\Omega_m = 0.3$.

The parameter β^* is defined by

$$\beta^* \equiv f\sigma_{8,\text{NL}}/\sigma_8^b \quad (1)$$

where f is the dimensionless growth rate defined as $f = d \ln D / d \ln a$, with D representing the growth function of linear perturbations and a being the scale factor. In Λ -cold dark matter (Λ CDM), $f \approx \Omega_m^{0.55}$ (Bouchet et al. 1995; Wang & Steinhardt 1998), though in modified gravity theories this

index can differ from 0.55 (e.g. Dvali et al. 2000; Linder & Cahn 2007). The term σ_8^b refers to the typical fluctuation scale in the galaxy over-density field at a radius of 8 Mpc/ h (the ‘b’ denotes that it is measured from a biased tracer, galaxies). $\sigma_{8,\text{NL}}$ is the typical fluctuation scale of the non-linear matter field at a radius of 8 Mpc/ h . The value of σ_8^b in the 2M++ data has been measured by Westover (2007) to 0.98 ± 0.07 by fitting projected correlation functions to 2MRS galaxies (Huchra et al. 2012), whereas C15 measured $\sigma_8^b = 0.99 \pm 0.04$ by using the maximum-likelihood scheme of counts in cells within radial shells (Efstathiou et al. 1990). Thus, C15 together with peculiar velocity samples can be used to constrain the growth of structure or the S_8 parameter (see e.g. Boruah et al. 2020; Said et al. 2020). The value of β^* in case of C15 calibrated against LOSS, Foundation, 2MTF, and SFI++ has been previously studied extensively in Boruah et al. (2020).

2.1.2 Lilow et al.

In Lilow et al. (2024, hereafter L24), the density and peculiar velocity fields are also reconstructed using the 2MRS data, but with a machine learning approach, rather than linear theory. The neural network is trained on mock data derived from the Quijote N -body simulations (Villaescusa-Navarro et al. 2020), incorporating redshift-space distortions, galaxy bias, and selection effects that closely mimic the characteristics of the 2M++ catalogue. The trained model is subsequently applied to the 2M++ data. L24 assume cosmological parameters from the fiducial Quijote simulations: $\Omega_m = 0.3175$, $\Omega_b = 0.049$, $h = 0.6711$, $n_s = 0.9624$, $\sigma_8 = 0.834$. The single field is presented on a 128^3 grid with a box size of $400h^{-1}$ Mpc and a voxel size of $3.1h^{-1}$ Mpc.

2.1.3 CSiBORG

The CSiBORG suite is a set of cosmological N -body simulations that are constrained to match the 3D mass distribution of the local Universe. This is achieved by imposing initial conditions (ICs) on the density field derived from the BORG algorithm applied to 2M++. BORG produces a posterior of voxel-by-voxel densities at $z = 1000$ by applying a gravity forward model, redshift-space distortions, observational selection effects and a biasing prescription to the ICs before comparing to the galaxy number density field of 2M++ with a Poisson likelihood (Jasche & Wandelt 2013; Lavaux & Jasche 2016; Jasche & Lavaux 2019; Lavaux et al. 2019; Porqueres et al. 2019). Each CSiBORG box resimulates a single BORG posterior sample, and thus the variation across the full set permits quantification of the uncertainty in the dark matter field due to incomplete knowledge of the galaxy field and its relationship to the underlying density.

Here we employ two versions of the CSiBORG simulations, based on different versions of the BORG 2M++ ICs. The first suite, CSiBORG1, uses the BORG 2M++ ICs from Jasche & Lavaux (2019), while the second suite, CSiBORG2, is based on the updated BORG 2M++ ICs from Stopyra et al. (2024). Both versions of the ICs are constrained within the 2M++ region, covering a spherical volume with a radius of approximately $155h^{-1}$ Mpc centred on the Milky Way ($z \lesssim 0.06$), embedded in a box of 1000 Mpc. The regions outside the 2M++ volume are largely unconstrained due to catalogue selection

providing the expected long-range forces in a Λ CDM framework. The BORG algorithm models the density field on a 256^3 grid, yielding a spatial resolution of $2.65 h^{-1}$ Mpc.

The CSiBORG1 suite, first introduced in Bartlett et al. (2021), consists of 101 dark matter-only N -body simulations in a $677.7h^{-1}$ Mpc box centred on the Milky Way. The constrained ICs from BORG are linearly evolved to $z = 69$ and augmented with white noise within the constrained 2M++ region on a $2,048^3$ grid, achieving a spatial resolution of $0.33h^{-1}$ Mpc and a dark matter particle mass of $3 \times 10^9 h^{-1} M_\odot$. A buffer region of around $10h^{-1}$ Mpc surrounds the high-resolution region, ensuring a smooth transition to the unconstrained, low-resolution outer region. For this work, however, we use only 20 of these resimulations to reduce the computational cost, though we verify that our results are not significantly affected by using all 101 resimulations. The initial conditions are evolved to $z = 0$ using the adaptive mesh refinement code RAMSES (Teysier 2002). The CSiBORG1 suite adopts cosmological parameters from Planck Collaboration et al. (2014), with H_0 set according to the 5-year WMAP results combined with Type Ia supernova and baryon acoustic oscillation data (Hinshaw et al. 2009): $\Omega_m = 0.307$, $\sigma_8 = 0.8288$, $H_0 = 70.5$ km/s/Mpc, $n_s = 0.9611$, $\Omega_b = 0.04825$.

The CSiBORG2 suite follows a similar setup but uses newer BORG ICs (Stopyra et al. 2024), which use a more accurate gravity model: a 20-step COLA integrator (Tassev et al. 2013) instead of the 10-step particle mesh solver of CSiBORG1. This was shown to improve the agreement of cluster masses with observational data. The cosmological parameters for CSiBORG2 are based on (Planck Collaboration et al. 2020a), with lensing and baryonic acoustic oscillations: $\Omega_m = 0.3111$, $\sigma_8 = 0.8102$, $H_0 = 67.66$ km/s/Mpc, $n_s = 0.9665$, $\Omega_b = 0.049$. We resimulate 20 samples of the BORG posterior ourselves using Gadget4 (Springel et al. 2021). We note that Stopyra et al. (2024) already resimulated 20 steps of the BORG posterior, but without the zoom-in technique: the CSiBORG setup allows us to reach ~ 200 times better mass resolution in the constrained region. In both CSiBORG suites, we construct the $z = 0$ density and velocity fields from the particle snapshots using the smoothed-particle hydrodynamics (SPH) technique (Monaghan 1992; Colombi et al. 2007) and set the minimum number of points to smooth over to 32 (following Section IV.B.1 of Bartlett et al. 2022). We render the final fields in voxels of $0.7h^{-1}$ Mpc.

Unlike C15, which is derived independently of the growth factor and consequently of σ_8 , the derivations of the BORG-based reconstructions (and all others presented in this work) assume fixed values for Ω_m and σ_8 . They naturally account for the β^* factor of Eq. (1), which is effectively pinned to 1. However, to search for systematics in the reconstructions leading to a mismatch with the peculiar velocity data, we allow the velocity fields other than C15 to be scaled by a free parameter β , with the fiducial value of 1, similarly to the A_L parameter in cosmic microwave background (CMB) lensing (Calabrese et al. 2008). We retain the notation of β^* for the scaling factor of C15, who measured $\beta^* = 0.431 \pm 0.021$.

2.1.4 Sorce

The reconstructions presented in Sorce (2018, 2020, hereafter S18) employ the technique of constrained realisations.

S18 is based on the grouped version of the Cosmicflows-2 catalogue (CF2; Tully et al. 2013) containing $\sim 5,000$ objects, considerably fewer than the 2M++ catalogue. Moreover, unlike the reconstructions discussed previously, **S18** is constrained by peculiar velocities rather than by redshift-space positions of galaxies. Briefly, the peculiar velocities are first grouped to reduce non-linear motions, followed by a bias minimisation technique to address observational biases. The cosmic displacement field is then reconstructed using a Wiener filter, and constraints are repositioned to the locations of their progenitors via the reverse Zel’dovich approximation. This approach constrains the density field using observed peculiar velocities, supplemented by a Gaussian random field to statistically restore “missing” structures. The resulting ICs are enhanced with additional white noise to increase the resimulation resolution and are evolved to $z = 0$ using **Gadget2** (Springel 2005). We use a single simulation conducted in a $500h^{-1}$ Mpc box with a particle mass of $8 \times 10^{10}h^{-1} M_{\odot}$, assuming the cosmological parameters of Planck Collaboration et al. (2014). We construct SPH density and velocity fields from the particle snapshot, and render the final fields in voxels of size $0.7h^{-1}$ Mpc.

2.1.5 Courtois et al.

In Courtois et al. (2023, hereafter **C23**), the density and velocity fields of the local Universe below $z = 0.08$ are reconstructed using the grouped Cosmicflows-4 (CF4; Tully et al. 2023) catalogue, which includes distances and redshifts for 38,000 groups. Similarly to **S18**, the reconstruction of **C23** is constrained by peculiar velocities. It is performed via a forward-modelling procedure using an Hamiltonian Monte Carlo (HMC) algorithm to sample potential realisations of the density field at $z = 0$, along with other auxiliary parameters (see Graziani et al. 2019 for further details). Under the assumption of linear theory, the velocity field is then derived from the density field and compared to the peculiar velocity data. We use a version of the **C23** reconstruction with a grid resolution of 256^3 , corresponding to a voxel size of $3.9h^{-1}$ Mpc, and we use 20 samples from the posterior distribution.

2.1.6 Visual comparison

We show slices through the density field at $z = 0$ from the six reconstructions we consider in Fig. 1. **C15** and **L24** are qualitatively similar, but do not display significant cosmic web-like features. In contrast, the **CSiBORG** fields reveal a prominent cosmic web structure due to their use of non-linear modelling. This is true even after averaging the density field over 20 independent posterior samples, suggesting that it is not due to the unconstrained white noise of these simulations. The **C23** field appears more diffuse despite having a voxel resolution of $3.9h^{-1}$ Mpc (similar to **C15**), which suggests that despite the voxel resolution the field varies only at much larger scales. Lastly, while the field of **S18** is also constrained at the level of linear theory, it was resimulated at a much higher resolution with additional small-scale white noise, resulting in a clear cosmic web.

Unlike the **CSiBORG** reconstructions, the **S18** field is a single realisation and, thus, the cosmic web features are more

likely due to unconstrained, small-scale modes, not matching the actual local Universe. We also show the line-of-sight (LOS) velocity in the direction of the Virgo cluster in Fig. 2 as an illustration of the differences between the fields, with the bands indicating the standard deviation among the 20 realisations for the appropriate fields.

2.2 Peculiar velocity samples

We use the Tully–Fisher relation (TFR) and supernova samples to calibrate the flow models, which we now discuss in turn. We do not use absolute calibration of the distance tracers, so the zero-point of the distance indicators is degenerate with the Hubble constant. However, since we work in distance units of h^{-1} Mpc, our results are independent of H_0 except for its influence on the power spectrum of the reconstructions. We show the samples’ observed redshift distribution in the CMB frame in Fig. 3. Our method for extracting luminosity distance information from the TFR and SN data is described in Sec. 3.

2.2.1 Tully–Fisher samples

The TFR (Tully & Fisher 1977) is an empirical relation between the width of a spectral line of spiral galaxies W (typically the HI line tracing neutral hydrogen) as a measure of the galaxies’ rotation velocity, and absolute magnitude M as measure of their luminosity. We write the relation as

$$M = a_{\text{TFR}} + b_{\text{TFR}}\eta + c_{\text{TFR}}\eta^2, \quad (2)$$

where a_{TFR} , b_{TFR} , and c_{TFR} are the zero-point, slope and curvature, respectively, though the latter term is commonly neglected as the relation is fairly linear. We reparameterise the linewidth to introduce a parameter η such that

$$\eta = \log W - 2.5, \quad (3)$$

where W is in kms^{-1} . Henceforth, we refer to η as the linewidth. In the subsequent analysis we will jointly infer the TFR calibration parameters along with the intrinsic scatter σ_{TFR} . We use three TFR samples: 2MTF, SFI++ and CF4, which we now describe in turn.

2MTF: The 2MTF survey is an all-sky sample consisting of 2,062 galaxies with TFR data up to $z_{\text{CMB}} \approx 0.03$, with a K -band apparent magnitude limit of 11.25 (Masters et al. 2008; Hong et al. 2019). We utilise the 2MTF dataset compiled by Boruah et al. (2020), which removes duplicates from the SFI++ sample, uses only K -band magnitudes and retains only galaxies with linewidths within the range $-0.1 < \eta < 0.2$. This final sample contains 1,247 galaxies.

SFI++: The SFI++ catalogue is an all-sky sample consisting of 4,052 galaxies and 736 groups up to $z_{\text{CMB}} \lesssim 0.05$, without a strict apparent magnitude threshold (Masters et al. 2006; Springob et al. 2007). Here we use the galaxy-only sample curated by Boruah et al. (2020) and adopt I -band magnitudes, though we do not apply their strict linewidth selection because we allow for TFR curvature. The final sample contains 2,010 galaxies.

CF4: The CF4 TFR survey consists of 9,792 galaxies up to $z_{\text{CMB}} \lesssim 0.05$, without a strict apparent magnitude threshold (Kourkchi et al. 2020a,b), and is a subset of the

Model	Alias	Constraint Data	Resolution	Description
Carrick et al. (2015)	C15	2M++ redshift-space positions	$4 h^{-1}$ Mpc	Linear inverse modelling using luminosity-weighted galaxy density field.
Lilow et al. (2024)	L24	2M++ redshift-space positions	$3.1 h^{-1}$ Mpc	Machine learning inverse method trained on Quijote simulations.
Jasche & Lavaux (2019)	CSiBORG1	2M++ redshift-space positions	$2.6 h^{-1}$ Mpc	BORG forward model; simulations from Bartlett et al. (2021) .
Stopyra et al. (2024)	CSiBORG2	2M++ redshift-space positions	$2.6 h^{-1}$ Mpc	BORG forward model with an improved gravity model; simulations introduced here.
Sorce (2018, 2020)	S18	CF2 peculiar velocities	$1.9 h^{-1}$ Mpc	Constrained realisation with Wiener filter and reverse Zel'dovich approximation; restores structures statistically from peculiar velocities.
Courtois et al. (2023)	C23	CF4 peculiar velocities	$3.9 h^{-1}$ Mpc	HMC sampling of the density field at $z = 0$ constrained against peculiar velocities.

Table 1. Summary of local Universe reconstructions of the density and velocity fields investigated in this work.

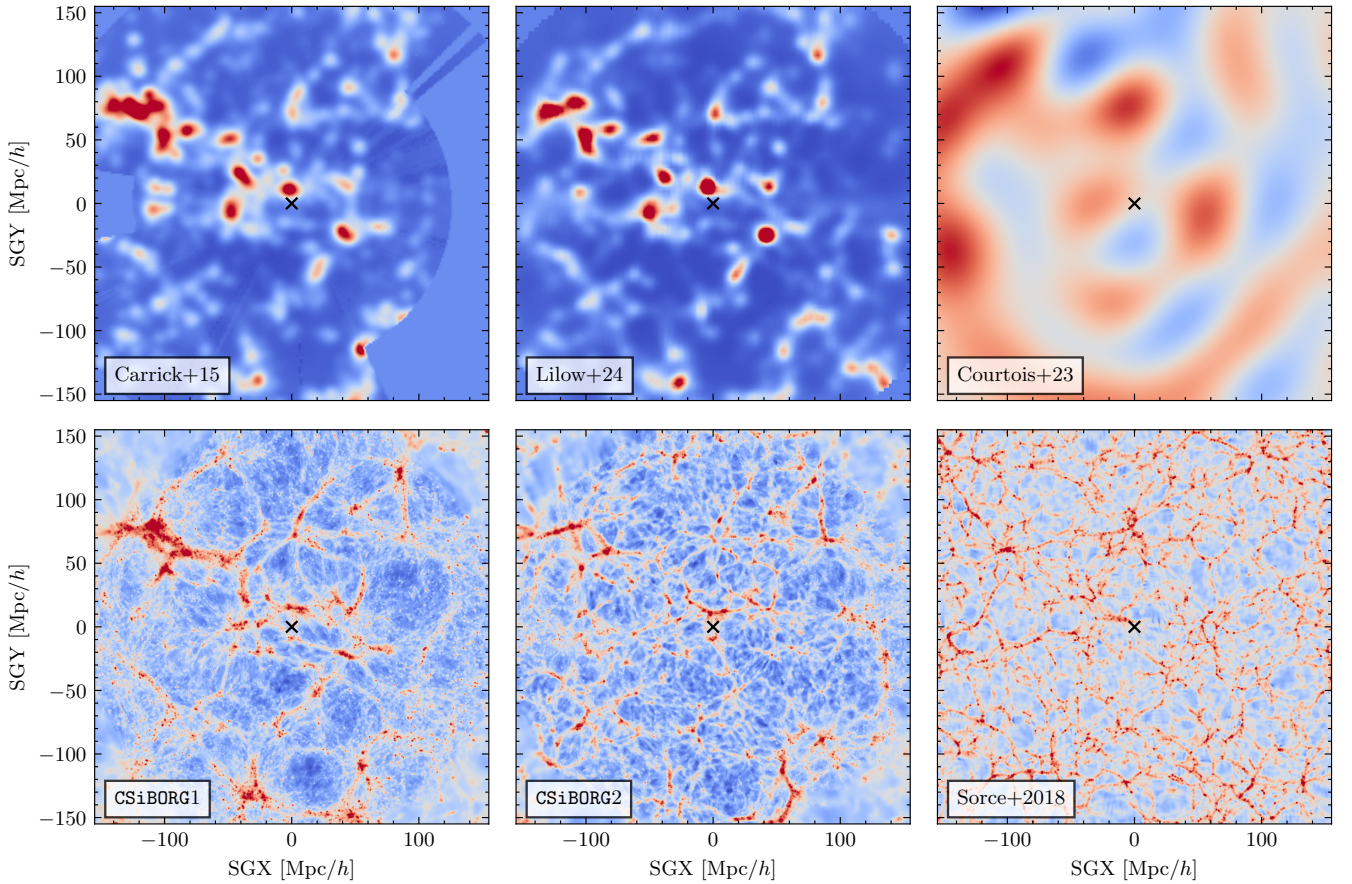


Figure 1. Slices of the density field in the SGX-SGY plane from $-155h^{-1}$ Mpc to $155h^{-1}$ Mpc in supergalactic coordinates at $z = 0$ for the local Universe reconstructions used in this work (Table 1). Redder (bluer) colours correspond to overdensities (underdensities). The density fields are presented without additional smoothing. For the fields in the bottom row we resimulated the ICs at higher resolution. The CSiBORG suites and [Courtois et al. \(2023\)](#) are averaged over 20 posterior samples. The black cross marks the origin, indicating the approximate position of the Local Group.

CF4 sample ([Tully et al. 2023](#)). We use both the SDSS i -band and WISE $W1$ magnitudes: while the former is limited to the SDSS footprint, the latter covers the entire sky. We treat the two bands as separate samples, though they are not independent, as some objects have both SDSS and WISE photometry. We retain objects already present in either the 2MTF or SFI++ samples, but select only galaxies with $\eta > -0.3$, galactic latitude $|b| > 7.5^\circ$ and quality flag 5 (best).

The final SDSS i -band and WISE $W1$ samples contain 5,027 and 3,278 galaxies, respectively. The publicly available CF4 catalogue does not list magnitude uncertainties, thus we set them to a fiducial (conservative) value of 0.05 mag ([Kourkchi et al. 2019](#)).

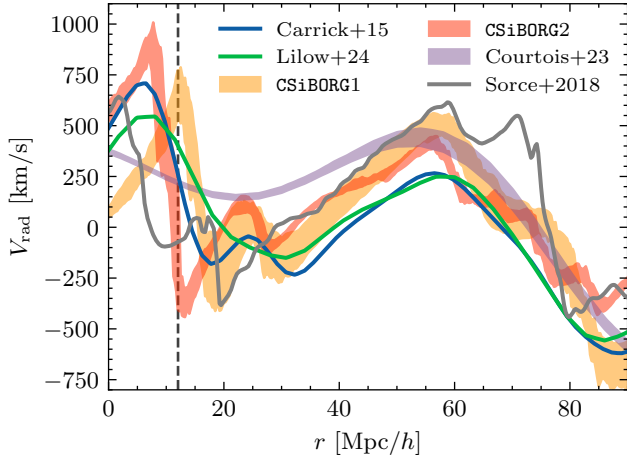


Figure 2. Examples of the reconstructed velocities along the LOS to the Virgo cluster, whose approximate distance is indicated by the dashed vertical line. For reconstructions providing multiple samples of the velocity field, a shaded region between 16th and 84th percentiles is shown. For Carrick et al. (2015) we assume the fiducial value of $\beta^* = 0.43$.

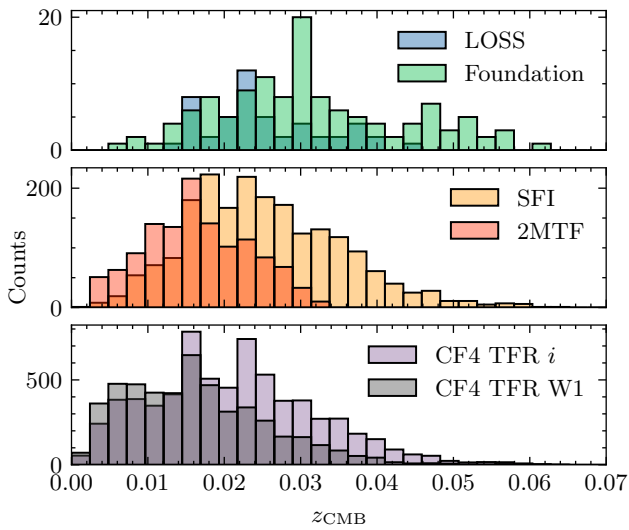


Figure 3. The distribution of observed redshifts converted to the CMB frame (z_{CMB}) for the peculiar velocity samples used in this work. With the exception of the Foundation sample, the majority lie within $z_{\text{CMB}} \lesssim 0.05$, while the 2MTF sample is constrained to $z_{\text{CMB}} \lesssim 0.03$ due to its magnitude limit. For visual clarity, the samples are arbitrarily separated into three rows, sharing the x -scale but each with its own y -scale.

2.2.2 Supernova samples

Supernova samples have been widely used as distance indicators in a variety of cosmological analyses. The SALT2 model standardises the supernova light curve (Guy et al. 2007), such that the “corrected” apparent magnitude m_{standard} , which relates the absolute magnitude and distance modulus in the usual way, can be written using the Tripp formula (Tripp 1998) :

$$m_{\text{standard}} = m_{\text{obs}} + \mathcal{A}x_1 - \mathcal{B}c. \quad (4)$$

Here, m_{obs} is the measured apparent magnitude and the last two terms act to standardise the supernova: x_1 is the stretch parameter describing the width of the light curve, and c is the supernova’s colour. m_{standard} together with the Type Ia supernova absolute magnitude M_{SN} determines the distance to the supernova. We take M_{SN} , \mathcal{A} and \mathcal{B} as global parameters of the fit separately for each supernova sample, which we infer jointly with the other model parameters defined below. Note that \mathcal{A} and \mathcal{B} are typically denoted α and β , but we have renamed them here to avoid confusion with variables defined later.

We use two supernova samples in this work: the Lick Observatory Supernova Search (LOSS; Li et al. 2000) and the Foundation Supernova Survey (Foundation; Foley et al. 2018; Jones et al. 2019). We adopt the curated samples from Boruah et al. (2020), where the LOSS sample is derived by Ganeshalingam et al. (2013). In this curation, supernovae already present in LOSS were removed from Foundation. The final LOSS and Foundation samples contain 55 and 125 supernovae, respectively. For discussion of our choice to use only these samples, and other samples that could potentially be used, see Section 5.5.

3 METHODOLOGY

In this section, we first explain the relationship between distance and redshift through peculiar velocities (Section 3.1). Next, we describe the probabilistic model used to infer the calibration parameters of the distance indicators and the velocity fields (Section 3.2). We then detail our approach to modelling selection effects in distance data (Section 3.3). Finally, we outline the method for computing the evidence of each model (Section 3.4).

3.1 Distance measures

The total redshift of a source in the CMB frame z_{CMB} is

$$1 + z_{\text{CMB}} = (1 + z_{\text{cosmo}})(1 + z_{\text{pec}}), \quad (5)$$

where z_{cosmo} is the redshift due to cosmic expansion and $z_{\text{pec}} = V_{\text{pec}}/c$ is the redshift produced by the radial peculiar velocity V_{pec} , also in the CMB frame. The cosmological redshift is related to the source comoving distance r as (e.g., Hogg 1999)

$$r(z_{\text{cosmo}}) = \frac{c}{H_0} \int_0^{z_{\text{cosmo}}} \frac{dz'}{\sqrt{\Omega_m(1+z')^3 + 1 - \Omega_m}}, \quad (6)$$

since we assume a flat Λ CDM universe dominated by non-relativistic matter and dark energy only, with Ω_m the matter density parameter. Within the single flow approximation, V_{pec} at the position of the source \mathbf{r} is

$$\mathbf{V}_{\text{pec}} = (\beta \mathbf{v}(\mathbf{r}) + \mathbf{V}_{\text{ext}}) \cdot \hat{\mathbf{r}}, \quad (7)$$

where $\hat{\mathbf{r}}$ is the unit vector along the source’s LOS and $\mathbf{v}(\mathbf{r})$ is the 3D velocity field evaluated at \mathbf{r} .

Eq. (7) introduces two new parameters for the velocity field, \mathbf{V}_{ext} which is the “external” velocity of the box, and β which is a scaling parameter. \mathbf{V}_{ext} is a constant vector accounting for the motion of the reconstruction box relative to the rest of the Universe, and is sourced by matter

Sample	Type	Number of objects	Description
2MTF	Tully–Fisher	1,247	Full-sky sample curated by Boruah et al. (2020) , retaining only linewidth range of $-0.1 < \eta < 0.2$ and with duplicates from the SFI++ sample removed.
SFI++	Tully–Fisher	2,010	Full-sky sample curated by Boruah et al. (2020) . No strict linewidth selection applied.
CF4 (SDSS <i>i</i> -band)	Tully–Fisher	5,027	Part of the CF4 survey, limited to the SDSS footprint. We retain only $\eta > -0.3$ and galactic latitude $ b > 7.5^\circ$.
CF4 (WISE <i>W1</i> -band)	Tully–Fisher	3,278	Part of the CF4 survey with full-sky coverage. Same selection criteria as the CF4 SDSS <i>i</i> -band sample.
Foundation	Type Ia supernova	125	Based on Foley et al. (2018) ; curated by Boruah et al. (2020) .
LOSS	Type Ia supernova	55	Based on Ganeshalingam et al. (2013) ; curated by Boruah et al. (2020) . Overlap with Foundation sample removed.

Table 2. Summary of the Tully–Fisher and supernova peculiar velocity samples used to test the velocity field reconstructions.

outside of this volume which cannot be picked up by the reconstructions themselves. β describes two effects. First, for the linear theory inverse reconstructions of [C15](#) where velocities are computed from the galaxy density field, then β is expected to be f/b where f is the dimensionless growth factor and b is the linear galaxy bias. In this case β contains important cosmological information. For the other reconstructions the velocities are derived from the matter field rather than the galaxy field, and hence this factor is not present and β is expected to be one. However, we keep it there as a measure of how reliably the reconstructions are matching the peculiar velocities implied by the data: if they are systematically over- or under-estimating these velocities we will find $\beta < 1$ or $\beta > 1$, respectively. A third parameter we introduce for each velocity field is σ_v , a Gaussian uncertainty between the field’s prediction and the “observed” value which is assumed to be position-independent. This describes to first order the effect of small-scale motions that cannot be captured by the velocity reconstruction methods. However, we note that [Hollinger & Hudson \(2024\)](#) showed on [C15](#)-like mock reconstructions that the recovered σ_v is inflated for galaxies near the Zone of Avoidance (which is masked in our catalogues). We refer to $\{\mathbf{V}_{\text{ext}}, \beta, \sigma_v\}$ collectively as “calibration” parameters of the fields.

The distance indicators typically relate an observable property to absolute magnitude M , which together with the apparent magnitude m yields an estimate of the distance modulus μ ,

$$\mu = m - M. \quad (8)$$

The distance modulus is a reparametrisation of the luminosity distance d_L ,

$$\mu = 5 \log \frac{d_L}{(1h^{-1} \text{Mpc})} + 25, \quad (9)$$

while d_L is related to comoving distance via

$$d_L = (1 + z_{\text{cosmo}})r. \quad (10)$$

3.2 Joint flow & distance calibration

We simultaneously calibrate both the distance indicator relation and auxiliary parameters associated with the density and velocity field, which we now introduce. We either use the provided density and radial velocity fields (in the case of [C15](#); [C23](#); [L24](#)) or construct them ourselves using SPH

from particle snapshots (for [CSiBORG1](#), [CSiBORG2](#), and [S18](#)). We evaluate these 3D fields along each tracer’s LOS up to radial distance of $175h^{-1}$ Mpc with a uniform spacing of $0.5h^{-1}$ Mpc, which is much higher than both the typical reconstruction resolution and distance uncertainty. We use the linear regular grid interpolator `RegularGridInterpolator` implemented in `scipy`¹ ([Virtanen et al. 2020](#)).

We wish to jointly infer the density and velocity field calibration $(\alpha, \beta, \sigma_v, \mathbf{V}_{\text{ext}})$, the distance indicator calibration $(a_{\text{TFR}}, b_{\text{TFR}}, c_{\text{TFR}}, \sigma_{\text{TFR}}$ for the TFR or $M_{\text{SN}}, \mathcal{A}, \mathcal{B}, \sigma_{\text{SN}}$ for supernovae), along with the Bayesian evidence for each model. We denote these parameters as θ and outline our model on the example of the TFR, though the supernova calibration is near-identical and we derive it in [Appendix A](#). For a TFR catalogue, the observables are the galaxy redshift converted to the CMB frame z_{CMB} , apparent magnitude m_{obs} , and linewidth η_{obs} . We also introduce two more latent parameters per object: the “true” apparent magnitude m_{true} and linewidth η_{true} . In the following, we omit the variables that the probabilities do not explicitly depend on to simplify the notation.

The model posterior is

$$\mathcal{P}(\theta, m_{\text{true}}, \eta_{\text{true}} | z_{\text{CMB}}, m_{\text{obs}}, \eta_{\text{obs}}) \propto \mathcal{L}(z_{\text{CMB}}, m_{\text{obs}}, \eta_{\text{obs}} | \theta, m_{\text{true}}, \eta_{\text{true}}) \pi(\theta, m_{\text{true}}, \eta_{\text{true}}), \quad (11)$$

where \mathcal{L} is the likelihood of the observables and π is the prior on the parameters. Implicitly, the likelihood also depends on the underlying density and velocity field, over which we later marginalise in [Eq. \(24\)](#). We expand the likelihood as

$$\mathcal{L}(z_{\text{CMB}}, m_{\text{obs}}, \eta_{\text{obs}} | \theta, m_{\text{true}}, \eta_{\text{true}}) = \int \mathcal{L}(z_{\text{CMB}} | \mu_{\text{true}}, \theta) p(\mu_{\text{true}}, \eta_{\text{obs}}, m_{\text{obs}} | \theta, m_{\text{true}}, \eta_{\text{true}}) d\mu_{\text{true}}, \quad (12)$$

bringing out the dependence on the true distance modulus of the galaxy μ_{true} . We numerically marginalise over μ_{true} using Simpson’s integration rule on a fixed grid implemented in `quadax`² ([Conlin 2024](#)). We generate points uniformly spaced in comoving distance with a spacing of $0.5h^{-1}$ Mpc which we

¹ <https://docs.scipy.org>

² <https://quadax.readthedocs.io>

convert to cosmological redshift or distance modulus using `Astropy`³ (Astropy Collaboration et al. 2013, 2018, 2022).

The first term in the integrand of Eq. (12) is the likelihood of the observed redshift given the true distance and the flow model. We now introduce the true redshift z_{true} and predicted redshift z_{pred} , where z_{pred} is a deterministic function of the true distance and the flow model (Eq. 5). This yields

$$\mathcal{L}(z_{\text{CMB}}|\mu_{\text{true}}, \boldsymbol{\theta}) = \int \mathcal{L}(z_{\text{CMB}}|z_{\text{true}}, \boldsymbol{\theta}) p(z_{\text{true}}|z_{\text{pred}}) dz_{\text{true}} dz_{\text{pred}}, \quad (13)$$

such that

$$\mathcal{L}(z_{\text{CMB}}|z_{\text{true}}) = \mathcal{N}(cz_{\text{CMB}}; cz_{\text{true}}, \sigma_{cz_{\text{CMB}}}), \quad (14)$$

where $\sigma_{cz_{\text{CMB}}}$ is the measurement uncertainty of the observed redshift, and

$$p(z_{\text{true}}|z_{\text{pred}}) = \mathcal{N}(cz_{\text{true}}; cz_{\text{pred}}, \sigma_v). \quad (15)$$

The true redshift is not equal to the predicted redshift if, for example, the velocity field has some finite resolution. The integral over z_{true} is done analytically and z_{pred} is a deterministic function of μ_{true} and the flow model, thus collapsing the integral to $z_{\text{pred}} = z_{\text{pred}}(\mu_{\text{true}}, \boldsymbol{\theta})$ such that

$$\mathcal{L}(z_{\text{CMB}}|\mu_{\text{true}}, \boldsymbol{\theta}) = \mathcal{N}\left(cz_{\text{CMB}}; cz_{\text{pred}}, \sqrt{\sigma_v^2 + \sigma_{cz_{\text{CMB}}}^2}\right). \quad (16)$$

The second term in the integrand of Eq. (12) is the joint distribution of the true distance and the TFR observables. The TFR provides an estimate of the distance modulus μ_{TFR} , defined as

$$\mu_{\text{TFR}} \equiv m_{\text{true}} - (a_{\text{TFR}} + b_{\text{TFR}}\eta_{\text{true}} + c_{\text{TFR}}\eta_{\text{true}}^2). \quad (17)$$

μ_{TFR} is not equal to the true distance in the model unless the TFR has no intrinsic scatter, i.e. $\sigma_{\text{TFR}} = 0$. We thus have

$$p(\mu_{\text{true}}, \eta_{\text{obs}}, m_{\text{obs}}|m_{\text{true}}, \eta_{\text{true}}, \boldsymbol{\theta}) = p(\mu_{\text{true}}|m_{\text{true}}, \eta_{\text{true}}, \boldsymbol{\theta}) \times p(m_{\text{obs}}, \eta_{\text{obs}}|m_{\text{true}}, \eta_{\text{true}}, \boldsymbol{\theta}), \quad (18)$$

where $p(\mu_{\text{true}}|m_{\text{true}}, \eta_{\text{true}}, \boldsymbol{\theta})$ is the conditional probability of the true distance given the TFR calibration, including a model for the Malmquist bias:

$$p(\mu_{\text{true}}|\eta_{\text{true}}, m_{\text{true}}, \boldsymbol{\theta}) = \frac{r^2(\mu_{\text{true}})n(\mu_{\text{true}})}{\mathcal{C}(\boldsymbol{\theta})} \frac{dr}{d\mu} \Big|_{\mu_{\text{true}}} \times \mathcal{N}(\mu_{\text{true}}; \mu_{\text{TFR}}, \sigma_{\text{TFR}}). \quad (19)$$

In this equation, r^2 accounts for the homogeneous Malmquist bias at the true distance to the tracer, i.e. the prior that galaxies are uniformly distributed in volume and hence are preferred to be at larger distance through the volume element scaling as r^2 . $n(\mu_{\text{true}})$ is a prior probability on the source number density at distance μ_{true} , accounting for inhomogeneous Malmquist bias, while $dr/d\mu$ accounts for the change of variables from real-space distance to distance modulus. Lastly, $\mathcal{C}(\boldsymbol{\theta})$ is a normalization constant that ensures that the distribution integrated over μ_{true} yields unity

and is computed as

$$\mathcal{C}(\boldsymbol{\theta}) = \int d\mu_{\text{true}} r^2(\mu_{\text{true}})n(\mu_{\text{true}}) \frac{dr}{d\mu} \Big|_{\mu_{\text{true}}} \times \mathcal{N}(\mu_{\text{true}}; \mu_{\text{TFR}}, \sigma_{\text{TFR}}). \quad (20)$$

To model $n(r)$ we assume a generic power-law bias model:

$$n(\mathbf{r}) \propto \rho(\mathbf{r})^\alpha \quad (21)$$

where ρ is the underlying density field of the reconstruction. The parameter α is jointly inferred from the data with a uniform prior, thus acting as another nuisance parameter in the inference. It is expected that $\alpha > 0$ because galaxies form at the peaks of the matter field. Note that for any linear bias of the form $n(r) = \alpha(\rho(r)/\rho_0)$ with some constant ρ_0 , the probability $p(\mu_{\text{true}}|\eta_{\text{true}}, m_{\text{true}}, \boldsymbol{\theta})$ would be independent of α due to its normalisation.

Finally, in Eq. (18) we have the conditional probability of the observed given the true TFR variables, which accounts for both the observational uncertainties and the selection effects. We assume that m_{obs} and η_{obs} are independent, so that

$$p(x_{\text{obs}}|x_{\text{true}}) = \frac{S(x_{\text{obs}})\mathcal{N}(x_{\text{obs}}; x_{\text{true}}, \sigma_x)}{\int S(x)\mathcal{N}(x; x_{\text{true}}, \sigma_x)dx}, \quad (22)$$

where x may refer to either m or η , S to their respective selection functions, and σ_x to their measurement uncertainties. We discuss the selection further in Section 3.3.

Bringing this all together produces the full likelihood:

$$\begin{aligned} \mathcal{L}(z_{\text{CMB}}, m_{\text{obs}}, \eta_{\text{obs}}|\boldsymbol{\theta}, m_{\text{true}}, \eta_{\text{true}}) = & \int dr \mathcal{N}\left(cz_{\text{CMB}}; cz_{\text{pred}}, \sqrt{\sigma_v^2 + \sigma_{cz_{\text{CMB}}}^2}\right) \\ & \times \frac{r^2 n(r) \mathcal{N}(\mu_{\text{true}}; \mu_{\text{TFR}}, \sigma_{\text{TFR}})}{\int r'^2 n(r') \mathcal{N}(\mu'_{\text{true}}; \mu'_{\text{TFR}}, \sigma_{\text{TFR}}) dr'} \\ & \times \frac{S(m_{\text{obs}})\mathcal{N}(m_{\text{obs}}; m_{\text{true}}, \sigma_m)}{\int S(m'_{\text{obs}})\mathcal{N}(m'_{\text{obs}}; m_{\text{true}}, \sigma_m) dm'_{\text{obs}}} \\ & \times \frac{S(\eta_{\text{obs}})\mathcal{N}(\eta_{\text{obs}}; \eta_{\text{true}}, \sigma_\eta)}{\int S(\eta'_{\text{obs}})\mathcal{N}(\eta'_{\text{obs}}; \eta_{\text{true}}, \sigma_\eta) d\eta'_{\text{obs}}}. \end{aligned} \quad (23)$$

This uses the true comoving distance rather than distance modulus, $r = r(\mu_{\text{true}})$, integrating over it numerically as described above. The inhomogeneous Malmquist bias term $n(r)$ makes analytical marginalisation over the latent variables $\mu_{\text{true}}, m_{\text{true}}$ intractable and we therefore sample them with HMC instead. When considering reconstructions with more than one possible realisation of the density and velocity field, we average the likelihood to marginalise over the reconstruction as

$$\begin{aligned} \mathcal{L}(z_{\text{CMB}}, m_{\text{obs}}, \eta_{\text{obs}}|\boldsymbol{\theta}, m_{\text{true}}, \eta_{\text{true}}) = & \int d\mathbf{v} d\rho \mathcal{L}(z_{\text{CMB}}, m_{\text{obs}}, \eta_{\text{obs}}|\boldsymbol{\theta}, m_{\text{true}}, \eta_{\text{true}}, \mathbf{v}, \rho) p(\mathbf{v}, \rho) \\ \approx & \frac{1}{N} \sum_i \mathcal{L}(z_{\text{CMB}}, m_{\text{obs}}, \eta_{\text{obs}}|\boldsymbol{\theta}, m_{\text{true}}, \eta_{\text{true}}, \mathbf{v}_i, \rho_i), \end{aligned} \quad (24)$$

where ρ_i and \mathbf{v}_i represent the i^{th} density and velocity field realisation, respectively, and $p(\mathbf{v}, \rho)$ is the probability of a given realisation (i.e. the posterior distribution from e.g. BORG). We approximate this as a discrete sum over the available realisations, giving each one the same probability. When

³ <https://www.astropy.org>

considering multiple galaxies, the likelihood becomes a product of the likelihoods of individual galaxies under the assumption of independence. In the case of a supernova calibration we treat the three independent variables (m , x_1 , c) analogously to the TFR observables, except for the supernova samples employed in this work we do not consider any selection (see Appendix A).

We use a Jeffreys prior on σ_v : $\pi(\sigma_v) \propto 1/\sigma_v$ and similarly for both σ_{TFR} and σ_{SN} . We set uniform priors on the both the TFR parameters (a_{TFR} , b_{TFR} and c_{TFR}) and the supernova calibration (M , x_1 and c). The external velocity \mathbf{V}_{ext} is sampled uniformly in both magnitude and direction. In case of the TFR, we use a Gaussian hyperprior for the true magnitude and linewidth,

$$\pi(m_{\text{true}}, \eta_{\text{true}} | \boldsymbol{\theta}) = \mathcal{N}(m_{\text{true}}, \eta_{\text{true}} | \boldsymbol{\mu}_{\text{TFR}}, \mathbf{C}_{\text{TFR}}), \quad (25)$$

where the mean is $\boldsymbol{\mu}_{\text{TFR}} = \{\widehat{m}, \widehat{\eta}\}$, which we infer with a uniform prior, and the 2-dimensional covariance \mathbf{C}_{TFR} has three terms: the width in magnitude, linewidth and their correlation. We infer the first two with a Jeffreys prior and the latter with a uniform prior between -1 to 1 . In case of supernovae, we have a Gaussian hyperprior whose covariance matrix is 3-dimensional instead. As we move from a 2- to 3-dimensional covariance matrix, it is no longer guaranteed that this prior will yield a positive semi-definite matrix, and thus unphysical covariance matrices could be produced. However, we find that these problematic cases are not encountered during our inferences. The approach of distinguishing between observed and true parameters, to which a Gaussian hyperprior is assigned, is analogous to Marginalised Normal Regression (Bartlett & Desmond 2023) which was shown to be an unbiased regression method, and also follows previous work in the field of supernova cosmology (March et al. 2011, 2014; Rubin et al. 2015; March et al. 2018; Rubin et al. 2023).

To sample the posterior we use the No U-Turns Sampler (NUTS; Hoffman & Gelman 2011) method of HMC, as implemented in the NumPyro package⁴ (Phan et al. 2019). We remove burn-in and use sufficient steps for the Gelman-Rubin statistic to be one to within 10^{-3} (Gelman & Rubin 1992). All model parameters, along with their priors, are summarised in Table 3.

3.3 Selection effects

The selection function modifies the conditional probability of the observed given the true variables of Eq. (22). We consider two kinds of selection, relevant for different samples: a fixed threshold and a ‘‘continuous’’ selection.

3.3.1 Magnitude threshold

The 2MTF sample has a K -band threshold in the observed apparent magnitude $m_{\text{th}} = 11.25$, such that

$$S_{\text{th}}(m_{\text{obs}}) = \begin{cases} 1 & \text{if } m_{\text{obs}} \leq m_{\text{th}}, \\ 0 & \text{otherwise.} \end{cases} \quad (26)$$

This turns Eq. (22) to a truncated Gaussian distribution in m_{obs} , which corrects for the fact that an observed galaxy

whose m_{true} is near the selection threshold could not have been observed with a magnitude fainter than the threshold.

3.3.2 Continuous selection function in magnitude

Other samples do not have a hard cutoff but instead lose sources with a probability that varies continuously with magnitude. For example, the CF4 TFR sample is limited by the HI flux which indirectly leads to an apparent selection in magnitude due to their correlation (Kourkchi et al. 2020a). However, since the TFR samples are often compiled from various instruments, directly modelling the HI flux limit is non-trivial.

We instead follow the empirical approach of Boubel et al. (2024b) to model the selection function, wherein the observed distribution of magnitudes is $p_{\text{obs}}(m) \propto S(m)p(m)$, where

$$\log S(m) = a(m - m_2)^2 - a(m_1 - m_2)^2 - 0.6(m - m_1) \quad (27)$$

for $m > m_1$, and $S(m) = 1$ otherwise. $p(m)$ is the underlying distribution of apparent magnitudes while $S(m)$ describes the loss of galaxies due to selection, which is simply given a flexible form as a function of m . Boubel et al. assume that the underlying distribution of magnitudes is $p(m) \propto 10^{0.6m}$ which can be derived by assuming a radial distribution of equal-magnitude objects proportional to r^2 in Euclidean space (Hubble 1926). However, we verify that this relation holds even in the case of a general luminosity function for apparent magnitudes brighter than some threshold magnitude m_{th} , as long as $m_{\text{th}} < \mu_{\text{max}} + \bar{M}$, where μ_{max} is the maximum distance modulus and \bar{M} the brightest magnitude.

We fit the parameters m_1 , m_2 , and a to the observed magnitudes by maximising the likelihood

$$\mathcal{L}(\{m\} | m_1, m_2, a) = \prod_n p_{\text{obs}}(m^{(n)}), \quad (28)$$

where the product runs over the apparent magnitudes of objects in the sample. We use HMC to sample the model, with uniform priors on the parameters. We report the constraints in Table 4. $S(m)$ is then used in Eq. (22). We find that our results are insensitive to the precise value of m_1 , m_2 , and a and hence we use their mean hereafter. This selection skews the conditional distribution of Eq. (22) towards brighter magnitudes whenever $m_{\text{obs}} > m_1$. Lastly, in case of the linewidth selection, we only consider a truncation in η_{obs} for the 2MTF and CF4 samples. We do not consider any selection for the supernova samples used in this work.

3.4 Evidence calculation

The model evidence \mathcal{Z} is defined as an integral of the product of the likelihood and prior over the parameter space

$$\mathcal{Z} = \int d\boldsymbol{\theta} \mathcal{L}(D | \boldsymbol{\theta}) \pi(\boldsymbol{\theta}), \quad (29)$$

where D is some data and $\boldsymbol{\theta}$ are the model parameters. Thus, the interpretation of \mathcal{Z} is that of a likelihood averaged over the prior. The ratio of the evidences for two models, known as the Bayes factor, quantifies the relative support of the data for one model over another and serves as the principal

⁴ <https://num.pyro.ai/en/latest/>

Parameter	Description	Prior
<i>Flow model parameters</i>		
\mathbf{V}_{ext}	External velocity vector	Uniform in both magnitude and direction
σ_v	Scatter between the observed and predicted redshifts	$\pi(\sigma_v) \propto 1/\sigma_v$
α	Galaxy power-law bias parameter	Uniform
β or β^*	Velocity field scaling parameter	Uniform
<i>Distance calibration parameters</i>		
$a_{\text{TFR}}, b_{\text{TFR}}, c_{\text{TFR}}$	TFR coefficients (zero-point, slope, and curvature)	Uniform
σ_{TFR}	TFR magnitude intrinsic scatter	$\pi(\sigma_{\text{TFR}}) \propto 1/\sigma_{\text{TFR}}$
$M_{\text{SN}}, \mathcal{A}, \mathcal{B}$	Supernova coefficients (absolute magnitude, stretch, and colour coefficients)	Uniform
σ_{SN}	Supernova magnitude intrinsic scatter	$\pi(\sigma_{\text{SN}}) \propto 1/\sigma_{\text{SN}}$
<i>TF galaxy / SN latent parameters</i>		
$m_{\text{true}}, \eta_{\text{true}}$	True TFR apparent magnitude and linewidth	$\mathcal{N}(\{m_{\text{true}}, \eta_{\text{true}}\} \boldsymbol{\mu}_{\text{TFR}}, \mathbf{C}_{\text{TFR}})$
$\boldsymbol{\mu}_{\text{TFR}}$	Mean of the TFR Gaussian hyperprior in apparent magnitude and linewidth	Uniform
\mathbf{C}_{TFR}	Covariance matrix of the TFR Gaussian hyperprior in apparent magnitude and linewidth	$\pi(\sigma_i) \propto 1/\sigma_i$ for standard deviations σ_i and uniform in correlation coefficients
$m_{\text{true}}, x_{1,\text{true}}, c_{\text{true}}$	True supernova apparent magnitude, stretch, and colour parameters	$\mathcal{N}(\{m_{\text{true}}, x_{1,\text{true}}, c_{\text{true}}\} \boldsymbol{\mu}_{\text{SN}}, \mathbf{C}_{\text{SN}})$
$\boldsymbol{\mu}_{\text{SN}}$	Mean of the supernova Gaussian hyperprior in apparent magnitude, stretch, and colour parameters	Uniform
\mathbf{C}_{SN}	Covariance matrix of the supernova Gaussian hyperprior in apparent magnitude, stretch, and colour parameters	$\pi(\sigma_i) \propto 1/\sigma_i$ for standard deviations σ_i and uniform in correlation coefficients

Table 3. Summary of the free parameters of our model and their priors.

Catalogue	m_1	m_2	a
SFI++	11.60 ± 0.70	12.95 ± 0.08	-0.233 ± 0.02
CF4 i band	12.01 ± 0.22	13.88 ± 0.03	-0.16 ± 0.01
CF4 $W1$ band	10.92 ± 0.31	13.47 ± 0.03	-0.12 ± 0.01

Table 4. Magnitude selection coefficients (as defined in Eq. 27) for the SFI++ and two CF4 TFR samples. 1σ uncertainties are given.

model-selection tool of Bayesian statistics, assuming the two models are equally likely *a-priori*.

The model introduced in Section 3.2 includes, in addition to the model parameters, two (three) latent variables per galaxy in the case of a TFR (supernova) catalogue. This increases the dimensionality of the parameter space to $\mathcal{O}(1000)$, making evidence calculation infeasible using standard methods such as nested sampling (Skilling 2006). Recently, machine learning-based methods for evidence calculation, such as **harmonic** (McEwen et al. 2021; Polanska et al. 2024) and *floZ* (Srinivasan et al. 2024), have been developed. While these methods have shown success in $\mathcal{O}(100)$ -dimensional parameter spaces, they have not yet been shown capable of handling the dimensionality that would be required for a full calculation here.

To circumvent this problem, we consider an alternative model in which we fix the true values of the independent variables to their observed values, effectively imposing a Dirac distribution prior on them. The observational uncertainties are then propagated not by marginalising over the true values but instead through first-order error propagation, summing them in quadrature with σ_{TFR} or σ_{SN} (also

the method of Boruah et al. 2020) as

$$\sigma_{\text{TFR}} \rightarrow \sqrt{\sigma_{\text{TFR}}^2 + \sigma_m^2 + b_{\text{TFR}}^2 \sigma_\eta^2} \quad (30)$$

and

$$\sigma_{\text{SN}} \rightarrow \sqrt{\sigma_{\text{SN}}^2 + \sigma_m^2 + \mathcal{A}^2 \sigma_{x_1}^2 + \mathcal{B}^2 \sigma_c^2}, \quad (31)$$

where σ_{x_1} and σ_c are the measurement uncertainties of the SALT2 supernova light curve parameters.

This approach reduces the dimensionality of the model to under 10, and incurs only a small systematic error if the intrinsic scatters of the scaling relations dominate over the measurement uncertainties. In Appendix B we compare explicitly the posteriors that the two methods generate, finding only small differences. We emphasise however that this approximation is only used for calculating evidences; all other results are based on the full model described in Section 3.2.

Now that the dimensionality of the parameter space is sufficiently low, we may confidently apply the **harmonic**⁵ package, which applies normalising flows and the harmonic estimator to calculate the model evidences directly from the HMC posterior samples (McEwen et al. 2021; Polanska et al. 2024). As can be seen from Eq. (29), the evidence depends on the chosen prior distributions (including the widths of uniform priors). However, in most cases we always compare models with the same parameters, in which case the widths of uniform priors are unimportant. The exception is the model of C15, which necessitates the additional velocity field scaling parameter β^* . Expanding the uniform prior on β beyond the range permitted by the likelihood reduces the

⁵ <https://github.com/astro-informatics/harmonic>

evidence. Given that the width of the posterior on β ranges from ~ 0.5 in the worst case to 0.05 in the best, tightening the prior to encapsulate only the posterior could improve the evidence by up to $20 - 200\times$, or $1.3 - 2.3$ on a base-10 logarithm scale. This is not significant given the differences in evidence between reconstructions.

4 RESULTS

We use the following methods to assess the relative goodness of the local Universe reconstructions summarised in Table 1:

- (i) Bayesian evidence comparison between the different reconstructions for each peculiar velocity (Section 4.1).
- (ii) The magnitude of the inferred σ_v (Section 4.2).
- (iii) Difference between the inferred β (see Eq. 7) and one in cases where the reconstructions are derived from the matter field (Section 4.3).
- (iv) Comparison of the inferred \mathbf{V}_{ext} and agreement of the reconstructed velocity at $r \rightarrow 0$ with the Local Group velocity in the CMB frame (Section 4.4 and Section 4.5).

The interpretation of these metrics is as follows. The evidence gives the relative probability of the data under the model, which as described above is the main goodness-of-fit statistic of Bayesian inference. (ii) describes the magnitude of residuals between the observed and predicted redshifts, which measures the accuracy of the model in the posterior region of parameter space. We will also show it to correlate well with the evidence. (iii) also indicates whether the predicted velocities are in broad agreement with the observations: if $\beta < 1$ then the velocities are over-predicted on average while if $\beta > 1$ they are under-predicted, a systematic bias in either case. Lastly, (iv) measures the velocity at which the data requires the reconstruction box to move relative to the CMB. A smaller \mathbf{V}_{ext} is preferred, especially when the reconstruction volume is large, as this implies that the velocities within the box are sufficient to account for the data. However, \mathbf{V}_{ext} depends on both the reconstruction and the peculiar velocity sample used to constrain it, and thus it can only serve as a qualitative comparison. The dependence on the reconstruction volume arises partly from the fact that if the velocities within the box are sourced solely by internal matter, their average will be zero when the entire box is enclosed. Consequently, the average enclosed velocity in the CMB frame (the bulk flow) at such radii is determined exclusively by \mathbf{V}_{ext} which we assume to be constant. The bulk flow magnitude follows a Maxwell-Boltzmann distribution in the Λ CDM model (see e.g. Appendix B of Davis et al. 2011). In Section 4.5 we also present and compare the radial dependence of the predicted bulk flows and in Section 4.6 we report constraints on the growth-rate of large-scale structure using C15 and the CF4 TFR samples.

In addition to using the individual peculiar velocity samples outlined in Table 2, we also construct a single joint dataset by combining the LOSS, Foundation, and both CF4 TFR samples. For the latter, we prioritise SDSS photometry when available. We do not include 2MTF or SFI++ in this joint catalogue as these were used in constructing CF4; all objects in our joint dataset therefore contain just one measurement per galaxy. We select only objects with $z_{\text{CMB}} < 0.05$ that are within the reconstructed volume.

4.1 Evidence comparison

In Fig. 4, we show the Bayesian evidences to compare the relative goodness-of-fit of reconstructions against the peculiar velocity samples. Since the absolute value of the evidence of a model is meaningless, we only show the differences of the logarithmic evidences $\Delta \log_{10} \mathcal{Z}$, relative to the model with the lowest evidence. The TFR samples have greater discriminating power (larger differences in $\log_{10} \mathcal{Z}$) compared to supernova samples, since despite their smaller intrinsic scatter, the supernova samples that we use contain significantly fewer objects. For all models except that of C15 we fix $\beta = 1$ for this calculation.

We find CSiBORG2 to be the best model across all peculiar velocity samples, with C15 typically ranking second and L24 third with only a small difference between them. Relative to these, the two reconstructions based on CosmicFlows, S18 and C23, are strongly disfavoured. When testing the joint supernova and TFR dataset, we find qualitatively similar results.

A possible driver of the evidence differences is the varying resolutions of the reconstructions. To isolate this effect, we consider smoothing all fields to a resolution of $7.8h^{-1}$ Mpc which is twice the voxel resolution of C23. This is achieved by applying a Gaussian kernel with a standard deviation of $\sqrt{(7.8h^{-1} \text{ Mpc})^2 - \sigma_0^2}$ to the densities and velocities, where σ_0 is the original resolution (voxel size) of the field. However, a Gaussian smoothing kernel a standard deviation σ_0 is not equivalent to a field with voxel resolution σ_0 , thus this ‘‘matching’’ of resolutions is only approximate. We then recalculate the evidences for the smoothed fields, showing the results as hatched bars in Fig. 4. This reduces the differences in $\log_{10} \mathcal{Z}$ between the reconstructions, and also causes C15 to become the preferred model although both CSiBORG fields continue to perform well. Interestingly, smoothing has a major detrimental effect on L24, indicating that the machine-learning enhancement of smaller scales is coming at a cost to the linear scales. Even after smoothing the CosmicFlows-based reconstructions remain strongly disfavoured. This indicates that the finer-grained information in the other reconstructions contains accurate information, and that the redshift-space positions of 2M++ galaxies afford better constraints than the peculiar velocities of CosmicFlows.

In Fig. 5 we investigate the effect of smoothing on C15 using the joint supernovae and TFR dataset. We plot both $\Delta \log_{10} \mathcal{Z}$ and σ_v as functions of smoothing scale R_{smooth} . As expected, the goodness-of-fit degrades with increasing smoothing scale. Notably, σ_v increases proportionally, suggesting it is a good indicator of goodness-of-fit. However, σ_v should not be compared between different peculiar velocity samples, as it depends on sample properties such as the relative prevalence of field and cluster galaxies. We infer from these results that the field of C15 would need to be smoothed with a scale of $R_{\text{smooth}} \approx 22 \text{ Mpc}/h$ to match the evidence of C23, since we find $\Delta \log_{10} \mathcal{Z}$ of 890 between C15 and C23.

4.2 Magnitude of redshift residuals

We now turn to σ_v , which measures the residuals between the observed and predicted redshifts. This contains infor-

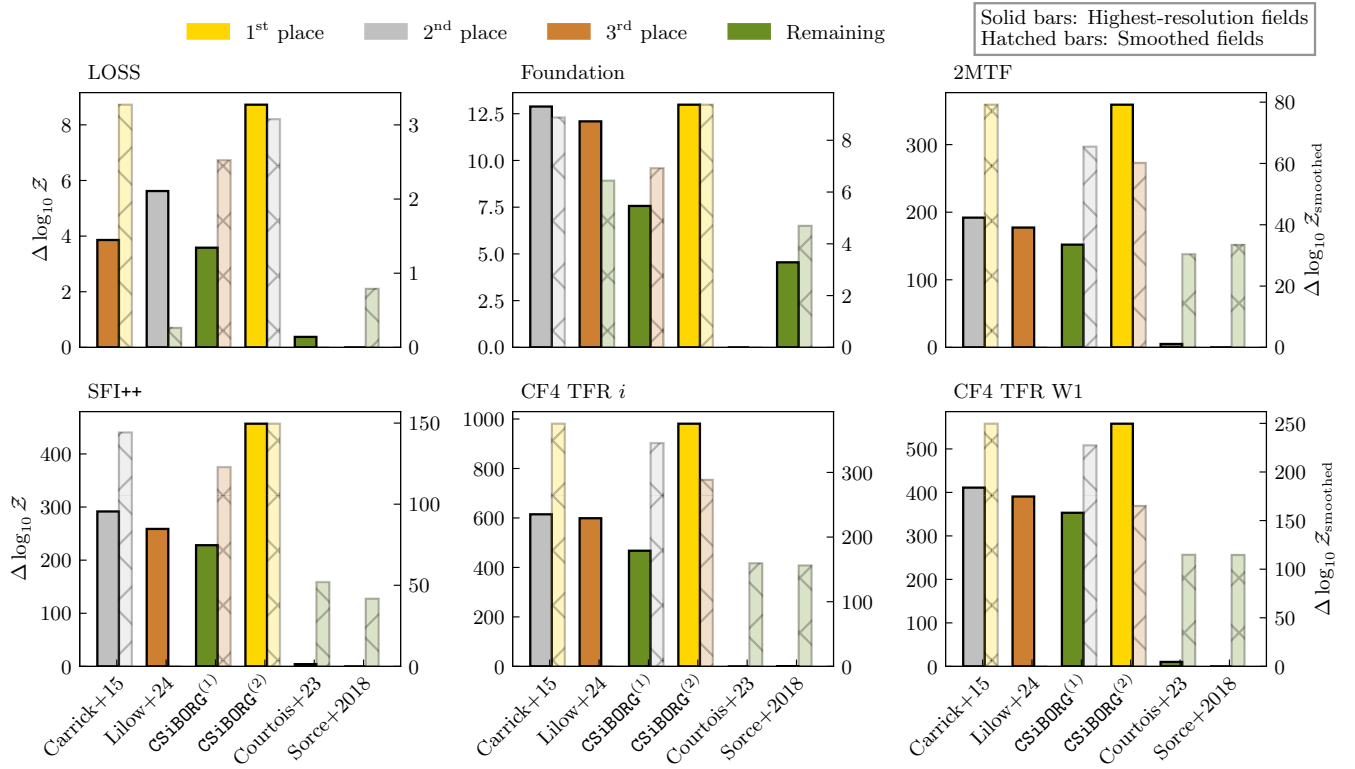


Figure 4. Differences in logarithmic evidences \mathcal{Z} from our flow validation model for various local Universe reconstructions (shown on the x -axis, see Table 1), compared against peculiar velocity samples (individual panels, see Table 2). Higher bars indicate a preferred model, and a bar of zero height indicates the reference (least successful) model. The logarithmic evidences are normalised with respect to the reference model as only relative differences are meaningful. Solid bars show evidences using the highest available resolution for each model, while hatched bars show evidences when all fields are smoothed to the resolution of $7.8h^{-1}$ Mpc, twice that of [Courtois et al. \(2023\)](#). Overall, **CSiBORG2** is the preferred model while the CosmicFlows-based reconstructions ([Sorce 2018](#) and [Courtois et al. 2023](#)) are disfavoured. Upon smoothing, the linear reconstruction of [Carrick et al. \(2015\)](#) becomes marginally preferred.

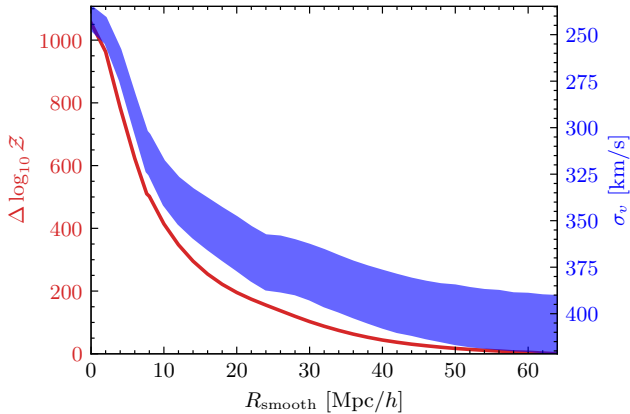


Figure 5. Differences in logarithmic evidence ($\Delta \log_{10} \mathcal{Z}$, with higher values indicating a better goodness-of-fit) and inferred σ_v (scatter between observed and predicted redshifts) as functions of smoothing scale R_{smooth} for the joint supernova and TFR dataset against [Carrick et al. \(2015\)](#). The σ_v axis is inverted. Both the goodness-of-fit and σ_v quickly degrade with increased smoothing, indicating that σ_v is an effective goodness-of-fit indicator.

mation on how well the reconstruction reproduces the “observed” velocity field of the local Universe. σ_v depends on whether galaxy non-linear velocities were suppressed by

grouping. While it is preferable for σ_v to be lower, there must be a lower floor (per sample) describing the effect of small-scale motions that the reconstructed fields cannot hope to capture. This floor would be raised by any unaccounted-for systematic effects or other forms of model misspecification. From now on we employ the full likelihood of Eq. (23) rather than the approximate likelihood used for evidence calculation.

In Fig. 6 we present the constraints on σ_v using each of the velocity fields. Generally, reconstructions with lower σ_v values also achieve higher evidence scores, while those with higher σ_v are less favoured. However, the two supernova samples alone lack sufficient data to provide meaningful constraints on σ_v . For the TFR samples, it is notable that **C15** yields lower σ_v values compared to **L24**, consistent with the evidence comparison’s preference for **C15**. This appears to indicate that the “augmentation” to **C15** provided by machine learning is not particularly successful. Similarly, the **CSiBORG2** velocities produce the greatest evidences and often require the lowest σ_v , except for an unexpectedly low σ_v of $56 \pm 24 \text{ km s}^{-1}$ for **C15** on the SFI++ sample. This is considerably below the expected mismatch from non-linear motions of around 150 km s^{-1} (**C15**). However, when tested against SFI++ all reconstructions’ posteriors on σ_v extend to zero, suggesting a potential issue on the catalogue side.

In contrast, the reconstructions based on CosmicFlows

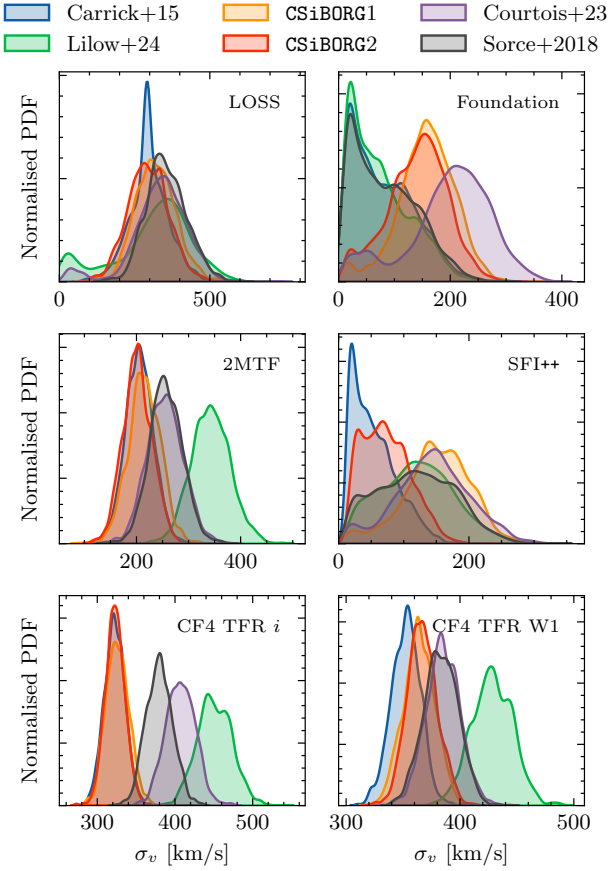


Figure 6. The posteriors on σ_v for each reconstruction applied to each dataset. As expected, reconstructions favouring lower σ_v tend to be preferred in terms of evidence as well (see Fig. 4). **CSiBORG2** and **Carrick et al. (2015)** produce the lowest σ_v values on the CF4 datasets, whereas **Courtois et al. (2023)** and **Sorce (2018)** prefer the largest values, despite being constrained by CosmicFlows data.

data require the highest σ_v , even for the CF4 samples. This outcome is surprising as these reconstructions are directly constrained by CosmicFlows data, of which the TFR samples are a subset. **C23** reported an inferred σ_v value of approximately 300 km s^{-1} when constraining their fields, yet our analysis yields higher values of $404 \pm 20 \text{ km s}^{-1}$ and $380 \pm 15 \text{ km s}^{-1}$ against the *i*- and *W1*-band CF4 samples, respectively.

4.3 Consistency of the velocity scaling

Next we examine β , which scales the velocity field before comparison to the data (Eq. 7). Here we treat β as a free parameter with a uniform prior, with the expectation that $\beta = 1$ for reconstructions where the velocities are sourced by the matter field; a field is better behaved to the extent that this is preferred *a posteriori*.

The constraints on β are shown in Fig. 7. We find that the model preferred by the Bayesian evidence, **CSiBORG2**, somewhat underpredicts velocities in the SFI++ and CF4 *i*-band samples, resulting in $\beta = 1.13 \pm 0.03$ and 1.14 ± 0.02 respectively. However, in our previous evidence comparison we had fixed $\beta = 1$, indicating that treating it as a free param-

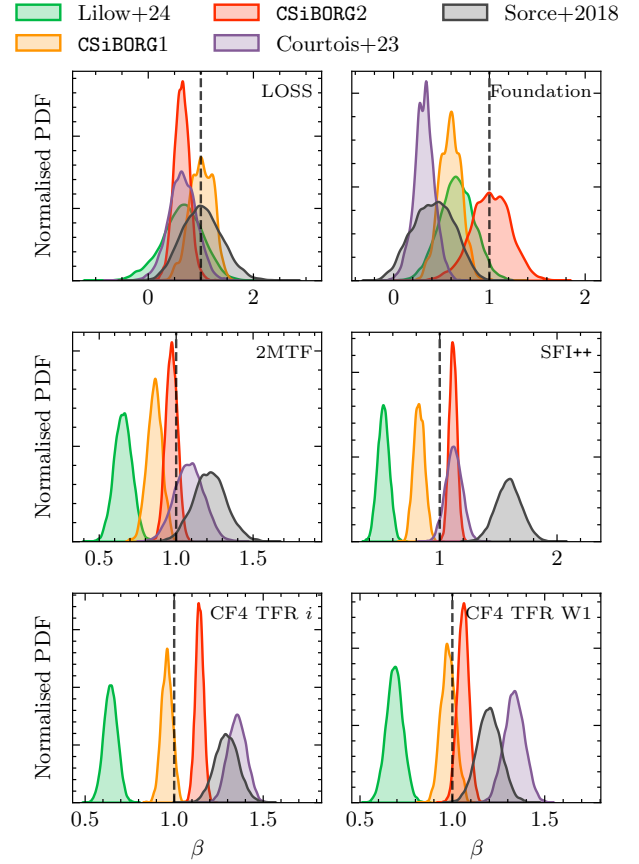


Figure 7. Inferred values of β (Eq. 7) given a uniform prior, for the models in which velocities are derived from the matter field. The fiducial value $\beta = 1$ is that at which the velocities prefer not to be rescaled. The CF4 TFR samples prefer high β values in all cases suggesting that its velocities are high relative to the other peculiar velocity samples. The exception is **Lilow et al. (2024)**, which, in contrast, shows systematically low β values across all datasets. This suggests that the **Lilow et al. (2024)** reconstruction overpredicts velocities.

ter would extend that model's lead. In contrast, **CSiBORG1** recovers β consistent with 1 in all cases except for SFI++, where β is low (0.82 ± 0.05). **L24** consistently produces $\beta < 1$ on all TFR samples, suggesting its reconstructed velocities are too high or otherwise systematically biased. On the other hand, **S18** has $\beta > 1$ on all TFR samples and **C23** is consistent with 1 for the SFI++ and 2MTF samples, but biased higher for the CF4 *i*-band and *W1*-band samples (1.35 ± 0.05 and 1.34 ± 0.06 , respectively). We leave a detailed discussion of β in **C15** to Section 4.6, as in **C15** it is directly related to the growth rate of large-scale structure.

4.4 Magnitude of the external velocity

Next we study $|\mathbf{V}_{\text{ext}}|$, the speed of the entire reconstruction box in the CMB frame sourced by matter outside it. This depends on both the reconstruction method and the peculiar velocity survey, which sets the effective probed volume.

The posteriors on $|\mathbf{V}_{\text{ext}}|$ are shown in Fig. 8. We observe that although **C15** and **L24** yield similar goodness-of-fit values, the latter requires a significantly smaller external flow

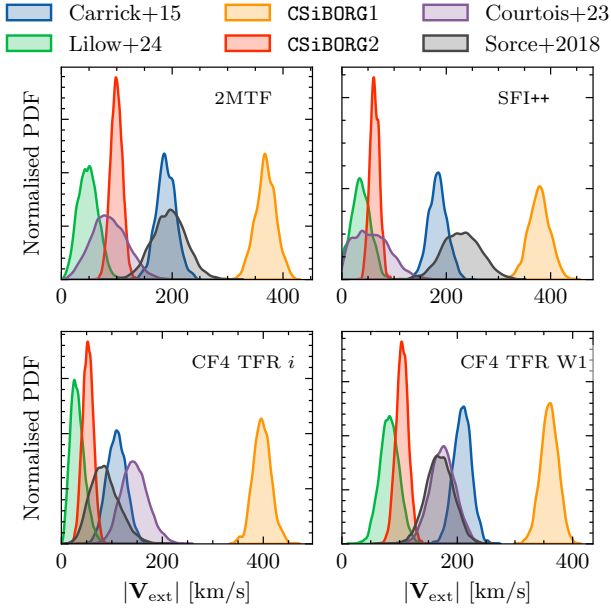


Figure 8. Inferred values of the magnitude of \mathbf{V}_{ext} (Eq. 7). A higher magnitude indicates that the reconstruction box is moving faster relative to the rest of the Universe.

despite both reconstructions being constrained by the same data. The external flow magnitude in L24 is nearly consistent with zero for the 2MTF, SFI++, and CF4 TFR i -band samples, with values of 49 ± 18 , 51 ± 16 , and 32 ± 14 km/s, respectively. In contrast, C15 requires larger magnitudes of 191 ± 17 , 190 ± 17 , and 109 ± 19 km/s for those samples.

Among the other reconstructions, CSiBORG2 generally requires the smallest external flow magnitude (~ 100 km s $^{-1}$), whereas CSiBORG1 typically requires a larger speed of approximately 400 km s $^{-1}$. For the CosmicFlows-based reconstructions, we find that their preferred flow magnitudes vary between the 2MTF and SFI++ samples, with S18 requiring a notably higher magnitude potentially due to the smaller depth of the CosmicFlows2 data used to constrain it. However, against the CF4 TFR samples, both S18 and C23 are generally consistent with each other, especially in the W1 band. Nevertheless, even in this case, the inferred magnitude of the external bulk flow remains relatively high, at 174 ± 22 km s $^{-1}$, compared to either CSiBORG2 or L24.

4.5 Bulk flow curve and Local Group velocity

Finally, we calculate the bulk flows produced by the various reconstructions. The velocities in each reconstruction are generated by the internal matter distributions and thus are in the “simulation” rest frame, where the average velocity of the box is 0 by definition. The exception to this is L24 whose neural network predicts both the density and velocity field, without explicitly computing the latter from the former and, thus, can learn “super-survey” scales encoded in the redshift-space distortions. This means that the L24 velocities already have \mathbf{V}_{ext} encoded in them, and hence the fiducial value for our free parameter is zero. We denote the simulation bulk flow as \mathbf{B}_{sim} and define it according to

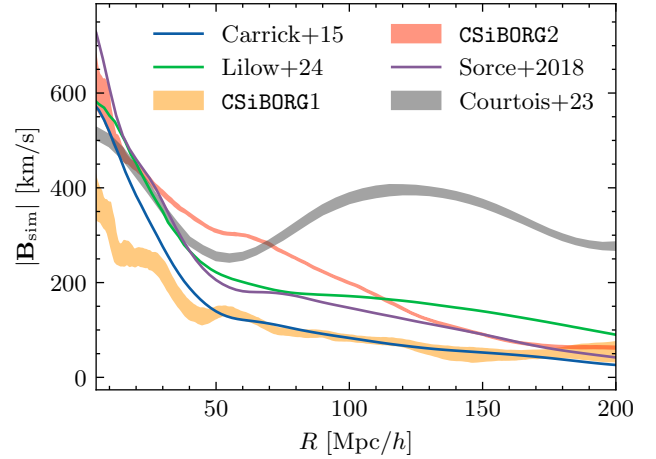


Figure 9. The bulk flow magnitude measured directly in the simulation rest frame (i.e., without considering additional \mathbf{V}_{ext}) as a function of radius R . All reconstructions, except for Courtois et al. (2023), exhibit a decreasing trend as expected in Λ CDM. For reconstructions that provide posterior samples, we plot the 16 $^{\text{th}}$ and 84 $^{\text{th}}$ percentiles as bands.

the standard bulk flow definition (Watkins et al. 2009; Feldman et al. 2010; Nusser & Davis 2011; Hoffman et al. 2015; Watkins & Feldman 2015; Nusser 2016; Scrimgeour et al. 2016; Feix et al. 2017; Hellwing et al. 2018; Peery et al. 2018; Whitford et al. 2023; Watkins et al. 2023)

$$\mathbf{B}_{\text{sim}}(R) = \frac{\beta}{V} \int_V \mathbf{v}(\mathbf{r}) dV, \quad (32)$$

where V is the volume enclosed within a sphere of radius R around the observer at the centre of each box. To calculate this we again set $\beta = 1$ for all reconstructions except C15, where we use the inferred posterior samples of β which we discuss in detail in Section 4.6.

We show the posterior predictive distributions of $\mathbf{B}_{\text{sim}}(R)$ in Fig. 9. All reconstructions except for C23 display a decreasing trend broadly consistent with the Λ CDM expectation. However, this is already partially enforced during the reconstruction process when a Λ CDM prior is applied: C15 uses a Λ CDM prescription to infer velocities from the galaxy density field, L24 uses a Λ CDM training set, BORG uses a Λ CDM prior on the ICs, C23 uses a Λ CDM prior on the $z = 0$ density field and linear theory to calculate velocities, and S18 assumes Λ CDM when constraining the ICs with the reverse Zel’dovich approximation. Most reconstructions show a bulk flow magnitude approaching approximately 600 km s $^{-1}$ near the origin, except for CSiBORG1, which reaches only ~ 400 km s $^{-1}$.

Next we study the radial dependence of the bulk flow in the CMB frame, which we calculate as

$$\mathbf{B}(R) = \mathbf{B}_{\text{sim}}(R) + \mathbf{V}_{\text{ext}}. \quad (33)$$

Note that this exhibits radial variation only within the reconstruction box: beyond it $\mathbf{B}(R)$ equals the constant \mathbf{V}_{ext} .

In Fig. 10 we present the CMB frame bulk flow magnitude and direction in galactic coordinates. We overplot the velocity of the Local Group in the CMB frame (on which more below) as well as the 1σ expectation for the bulk flow magnitude in Λ CDM using a top-hat window function of

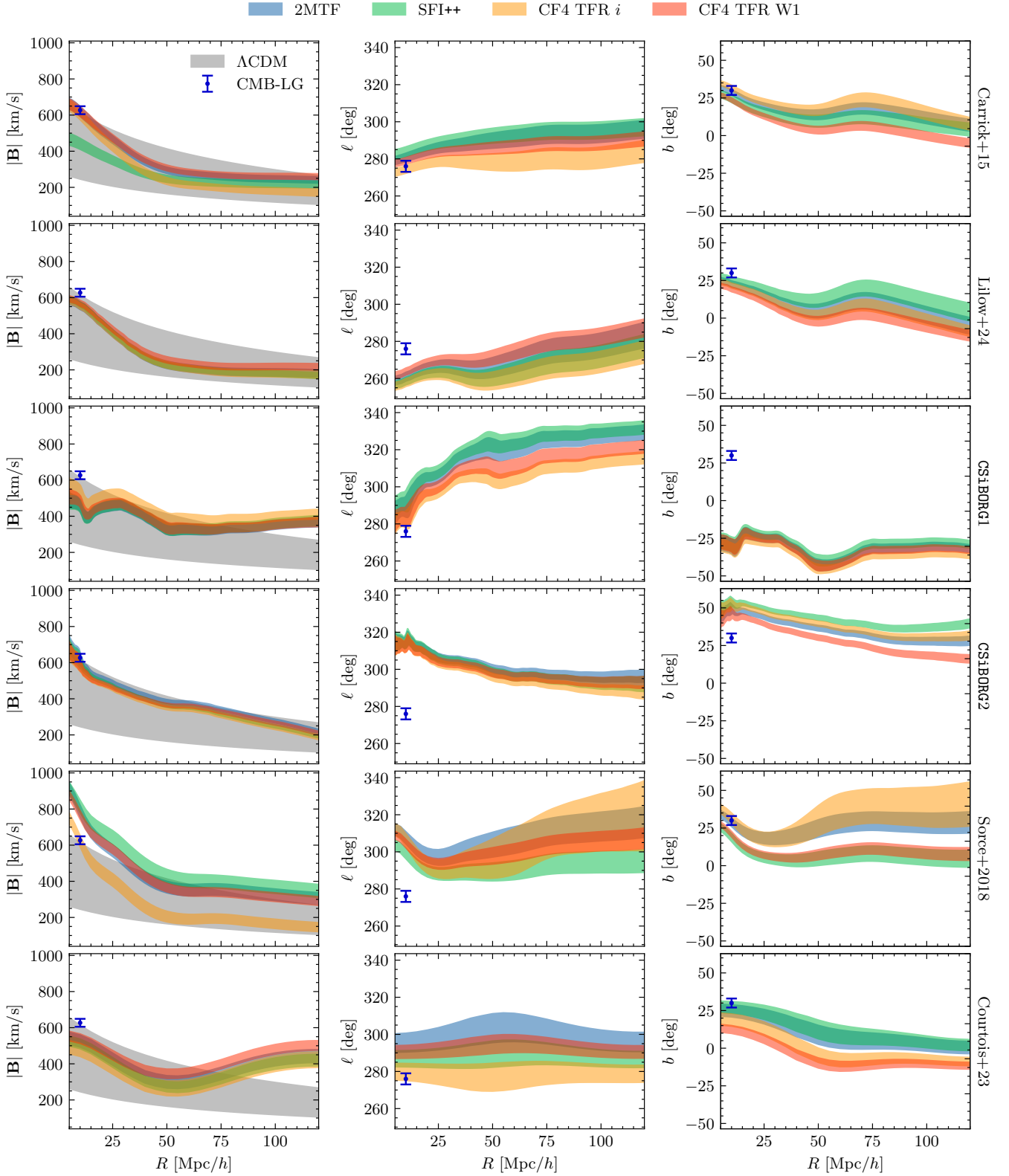


Figure 10. The bulk flow magnitude (left column) and direction in galactic longitude (l ; centre column) and latitude (b ; right column) as a function of radial distance for each reconstruction (rows). The bulk flow is computed as $B_{\text{sim}} + V_{\text{ext}}$, where B_{sim} is the bulk flow within each box (Fig. 9), and V_{ext} is the external velocity constrained by the displayed peculiar velocity samples. The grey band represents the 16th to 84th percentile range for the bulk flow magnitude expected in Λ CDM, while the single dark blue 1σ error bar indicates the motion of the Local Group in the CMB frame (Planck Collaboration et al. 2020a). This is plotted slightly offset from $R = 0$ simply for visual clarity.

radius R (see e.g. Sec. 6.1.2 of [Boruah et al. 2020](#)). We find that the bulk flow magnitude for most reconstructions aligns well with the Λ CDM expectation. This is not true for for **CSiBORG1** and **C23**, however, which overpredict the bulk flow at large R . In **CSiBORG1** this is driven by the large $|V_{\text{ext}}|$ (Fig. 8), while for **C23** it is driven by the large internal bulk flow (Fig. 9). Although this trend does not indicate significant tension with Λ CDM at the radii we probe ($\lesssim 150$ Mpc/h), Fig. 3 of [Courtois et al. \(2023\)](#) shows that their bulk flow appears to continue increasing beyond the radii we plot, posing a greater challenge to Λ CDM if true. This is also evident in [Watkins et al. \(2023\)](#), based on the same data.

Examining the bulk flow direction as a function of radial distance, we observe that the reconstructions of **C15** and **L24** display similar trends, though they do differ in longitude. The two **CSiBORG** reconstructions show significant disagreement in latitude. This disagreement between the two **BORG** reconstructions is not entirely surprising. The IC inference of **CSiBORG1** used an inferior gravity model and a different galaxy bias model ([Stopyra et al. 2024](#)), leading to an overestimation of cluster masses, which in turn should affect the local velocity field. This is reflected in the evidence comparison, where **CSiBORG1** is strongly disfavoured relative to **CSiBORG2**. Finally, the CosmicFlows-based reconstructions demonstrate similar directional trends, but the preferred V_{ext} varies significantly between the peculiar velocity samples leading to more prominent differences in bulk flow direction across samples.

Finally we investigate consistency with the one piece of information we have about the bulk flow curve: that the velocity of the Local Group (LG) in the CMB frame is 620 ± 15 km s $^{-1}$ towards $(\ell, b) = (271.9^\circ \pm 2.0^\circ, 29.6^\circ \pm 1.4^\circ)$, as inferred from the CMB dipole ([Planck Collaboration et al. 2020a](#)). To recover the predicted LG velocity B_{LG} , we evaluate the velocity fields at the origin to obtain $B_{\text{sim}}(R=0)$ and add to it V_{ext} . However, this cannot be directly compared to the observed CMB-LG velocity due to the σ_v scatter describing a point-by-point mismatch between predicted and observed velocities. To account for this we calculate B_{LG} as

$$B_{\text{LG}} = B_{\text{sim}}(R=0) + V_{\text{ext}} + V_{\text{rand}}, \quad (34)$$

where V_{rand} is a random vector with components drawn from a mean-zero Gaussian with standard deviation σ_v in each component. The result is shown in Fig. 11.

We find that propagating the σ_v uncertainty significantly broadens the uncertainties on the predicted LG motion compared to when this scatter is not included, since its value is comparable to the LG-CMB speed. Additionally, the variations between the different peculiar velocity samples, each with its specific V_{ext} and σ_v , are no longer significant. Therefore, in Fig. 11 we present the predicted LG motion for the CF4 TFR *W1* sample only, which is representative of all samples' results. We find agreement with the observed CMB-LG velocity in both magnitude and direction for all models; the only minor tension is found in **CSiBORG1**, where the predicted latitude deviates from the CMB dipole by $\sim 2\sigma$ ($-22^\circ \pm 21^\circ$).

4.6 Growth rate measurement

In the reconstruction of **C15**, the posterior samples on β^* , the velocity scaling parameter, are related to the parameter combination $f\sigma_{8,\text{NL}}$ through Eq. (1). As many cosmological probes measure the amplitude of the linear field $\sigma_{8,\text{L}}$, we wish to convert this to $f\sigma_{8,\text{L}}$. A mapping between $\sigma_{8,\text{NL}}$ and $\sigma_{8,\text{L}}$ was derived in [Juszkiewicz et al. \(2010\)](#), but we derive an alternative mapping using the non-linear matter power spectrum. To this end, we first obtain $\sigma_{8,\text{NL}}$ from $f\sigma_{8,\text{NL}}$ by using the approximation $f \approx \Omega_m^{0.55}$ ([Wang & Steinhardt 1998](#)). For all these conversions, we assume a flat Λ CDM with the cosmological parameters $h = 0.6766$, $\Omega_m = 0.3111$, $\Omega_b = 0.02242/h^2$ and $n_s = 0.9665$, except the amplitude of the primordial power spectrum A_s which we wish to infer. This is achieved by running a root-finding algorithm, where, for a given A_s , $\sigma_{8,\text{NL}}$ is computed by performing the appropriate integral of the non-linear matter power spectrum, which is evaluated using the **syren-new** emulator⁶ ([Bartlett et al. 2024](#); [Sui et al. 2024](#)). Once the corresponding value of A_s has been obtained, this is converted to the linear value of $\sigma_{8,\text{L}}$ using the conversion given in Eq. 5 of [Sui et al. \(2024\)](#). For our chosen cosmological parameters, we find a correction to the mapping previously derived by [Juszkiewicz et al. \(2010\)](#): the non-linear matter power spectrum-based mapping from $\sigma_{8,\text{NL}}$ to $\sigma_{8,\text{L}}$ is approximately 3% lower than reported by [Juszkiewicz et al.](#). The exact value of the discrepancy ranges from approximately 3-5%, depending on the exact non-linear prescription used. For example, using the [Mead et al. \(2016\)](#) implementation of **hmcode** gives a value which is 5% lower than the [Juszkiewicz et al.](#) formula. We choose to report values using the **syren-new** approximation of the non-linear power spectrum for this conversion due to its better agreement with N -body simulations ([Bartlett et al. 2024](#); [Sui et al. 2024](#)) compared to **hmcode** and **halofit** ([Smith et al. 2003](#); [Takahashi et al. 2012](#)). We show this mapping in Fig. 12. Similarly, [Hollinger & Hudson \(2024\)](#) derived the non-linear to linear σ_8 mapping using **halofit** ([Smith et al. 2003](#); [Takahashi et al. 2012](#)) and reported comparable disagreements with the results of [Juszkiewicz et al. \(2010\)](#).

In Fig. 13, we compare our measurements of β^* to various previous calibrations of **C15**. We find $\beta^* = 0.392 \pm 0.0146$ for the joint sample (LOSS+Foundation+CF4 TFR *i*-band+CF4 TFR *W1*-band). This value is similar to the *W1*-band-only measurement of $\beta^* = 0.396 \pm 0.0200$ but lower than the *i*-band-only result: $\beta^* = 0.431 \pm 0.0204$. The joint sample includes approximately twice as many data points, which, as expected, reduces the uncertainty in β^* by roughly a factor of $\sqrt{2}$.

As shown in Fig. 13, our measurement is lower than those reported by [Carrick et al. \(2015\)](#) and [Boruah et al. \(2020\)](#) but higher than the values from [Said et al. \(2020\)](#) and [Boubel et al. \(2024a\)](#). The difference is particularly noteworthy for [Boubel et al. \(2024a\)](#), who also used the CF4 TFR sample, suggesting some inconsistency. Using the **PosteriorAgreement** package⁷ (see Sec. 3.5 of [Bocquet et al. 2019](#)), we quantify the tension between our joint constraint on β^* and that of [Boruah et al. \(2020\)](#) as 1.9σ . Our *W1*-band-only measurement is consistent with ([Boubel et al.](#)

⁶ https://github.com/DeaglanBartlett/symbolic_pofk

⁷ <https://github.com/SebastianBocquet/PosteriorAgreement>

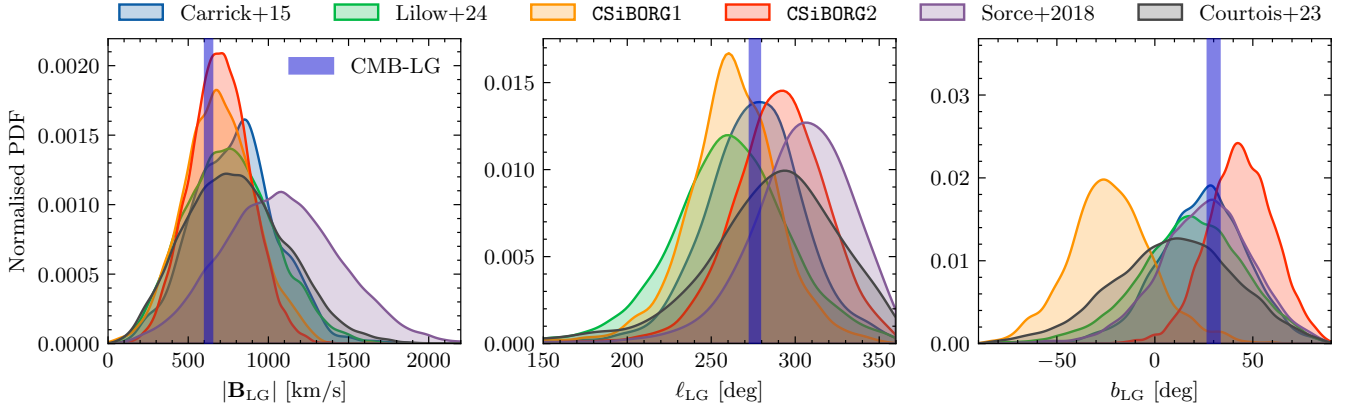


Figure 11. The predicted LG velocity following Eq. (34), where we propagate the σ_v noise. We show its magnitude, longitude and latitude ($|\mathbf{B}_{\text{LG}}|$, ℓ_{LG} , b_{LG}) in the CMB frame in galactic coordinates calibrated against the CF4 TFR W1-band sample for the various reconstructions. All predicted LG velocities are consistent with the observed CMB-LG velocity (1σ region in dark blue rectangles, Planck Collaboration et al. 2020a), although CSiBORG1, shows a $\sim 2\sigma$ deviation in latitude.

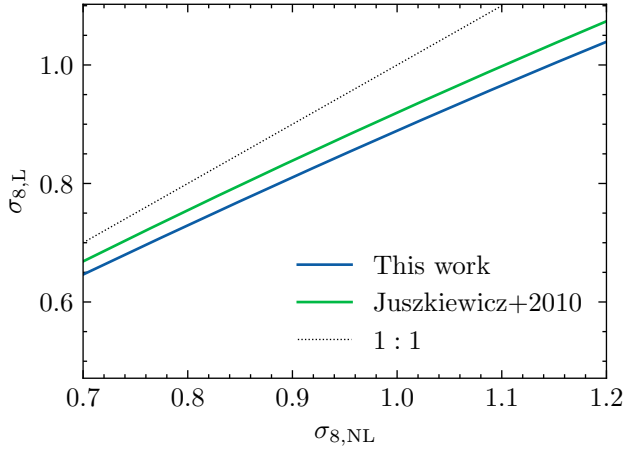


Figure 12. The mapping from $\sigma_{8,\text{NL}}$, the amplitude of density fluctuations computed using the non-linear matter power spectrum compared to the linearly evolved $\sigma_{8,\text{NL}}$. For our choice of cosmological parameters ($h = 0.6766$, $\Omega_m = 0.3111$, $\Omega_b = 0.02242/h^2$ and $n_s = 0.9665$), we find that the resulting $\sigma_{8,\text{L}}$ is $\sim 3\%$ lower than the one derived by Juskiewicz et al. (2010).

2024a) at 1.3σ , while the i -band-only result shows mild disagreement at 2.7σ .

Finally, we transform the posterior samples of β^* into $S_8 \equiv \sigma_{8,\text{L}}\sqrt{\Omega_m}/0.3$. Using the value of β^* calibrated on the joint sample, we find $S_8 = 0.69 \pm 0.034$ under the assumption that $\Omega_m = 0.3111$, based on the mapping of σ_8 described above. In contrast, applying the mapping of Juskiewicz et al. (2010) yields $S_8 = 0.71 \pm 0.035$ for the same value of β^* . Since our joint β^* is lower than that of Boruah et al. (2020) but higher than Said et al. (2020), we obtain correspondingly lower and higher S_8 values, though the tension remains insignificant. Assuming Ω_m values of either 0.25 or 0.35 alters our results by less than 1%.

In Fig. 14 we compare the inferred S_8 to various values from the literature. Our results are not in strong tension with other peculiar velocity measurements of S_8 (e.g. Huterer et al. 2017; Nusser 2017; Boruah et al. 2020;

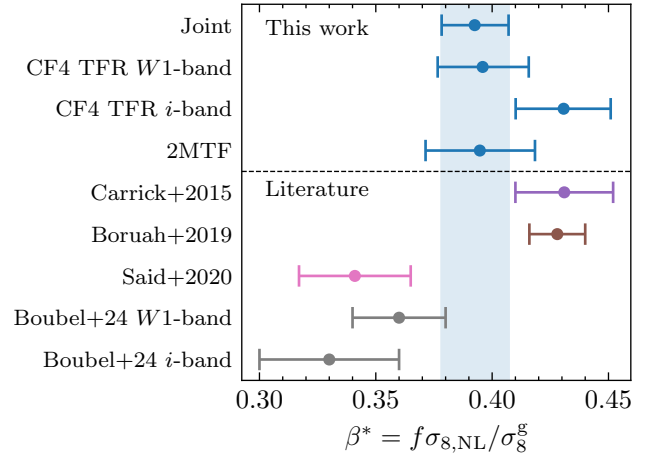


Figure 13. The velocity field scaling parameter β^* of Carrick et al. (2015) calibrated against various peculiar velocity samples, compared to previous literature calibration (Carrick et al. 2015; Boruah et al. 2020; Said et al. 2020; Boubel et al. 2024a). Joint indicates LOSS+Foundation+CF4 TFR W1-band+CF4 TFR i -band and the errors are 1σ .

Said et al. 2020). For instance, we find only a 1.7σ disagreement with Boruah et al. (2020), who employed the mapping of Juskiewicz et al. (2010) which we have shown to overestimate $\sigma_{8,\text{L}}$, and thus S_8 , by approximately 3%. In contrast, our constraint is in 2.5σ tension with the weak lensing results of Dark Energy Survey and Kilo-Degree Survey Collaboration et al. (2023) and 4.1σ tension with Planck TT,TE,EE+lowE+lensing (Planck Collaboration et al. 2020b). For example, the latter tension decreases to 1.9σ when β^* is inferred exclusively from the CF4 TFR i -band sample. Hollinger & Hudson (2024) used mock 2M++ realisations in conjunction with (smaller than CF4) mock TFR catalogues to show that the sample variance in $f\sigma_{8,\text{NL}}$ is approximately 5%. However, even incorporating this additional 5% uncertainty into the S_8 constraint reduces the tension with Planck only from 4.1σ to 2.7σ .

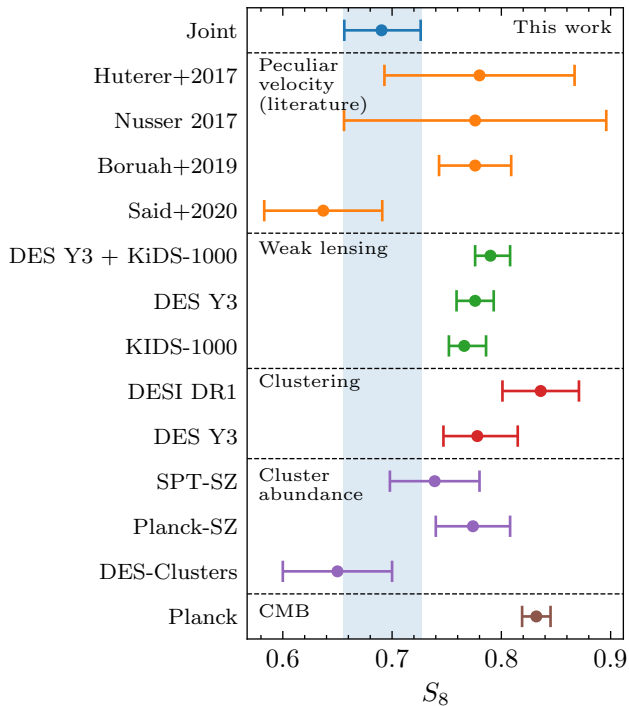


Figure 14. The $S_8 \equiv \sigma_{8,L} \sqrt{\Omega_m/0.3}$ parameter inferred from Carrick et al. (2015) calibrated against the joint peculiar velocity sample (LOSS+Foundation+CF4 TFR W1-band+CF4 TFR *i*-band). We compare to literature results using peculiar velocities (Huterer et al. 2017; Nusser 2017; Boruah et al. 2020; Said et al. 2020), weak lensing (Dark Energy Survey and Kilo-Degree Survey Collaboration et al. 2023; Abbott et al. 2022; Heymans et al. 2021), clustering (DESI Collaboration et al. 2024; Porredon et al. 2022), cluster abundance (Bocquet et al. 2019; Planck Collaboration et al. 2016; Abbott et al. 2020) and Planck TT,TE,EE+lowE+lensing (Planck Collaboration et al. 2020b). The errors are 1σ .

5 DISCUSSION

In this section, we provide a detailed summary of the results (Section 5.1), discuss their interpretation (Section 5.2), and address the caveats of our analysis (Section 5.3). We then compare our results with the literature (Section 5.4) and suggest possible future studies (Section 5.5).

5.1 Summary of results

We have evaluated several local Universe reconstructions using various peculiar velocity samples and metrics, ranging from a quantitative and to more qualitative analyses. Our first metric is the Bayesian evidence comparison of the reconstructions, shown in Fig. 4. This comparison consistently and strongly favoured CSiBORG2 over the other reconstructions. The second and third ranking reconstructions are those of C15 and L24, respectively, both of which, like CSiBORG2, are constrained using the 2M++ data. The earlier version of BORG, CSiBORG1, performs slightly worse than CSiBORG2, likely stemming from the fact that the ICs of CSiBORG2 were constrained using a more accurate, 20-step COLA gravity model, whereas the ICs of CSiBORG1 were based on a 10-step particle-mesh gravity model (for further details,

see Stopyra et al. 2024). In contrast, the CosmicFlows-based reconstructions of S18 and C23 consistently underperform when tested against both supernova and TFR samples. This outcome is particularly surprising when testing these reconstructions on the samples that were used to constrain them, for which the other models still perform better. We comment on this further in Section 5.3.

Previous studies typically set σ_v to 150 km s^{-1} based on a comparison to N -body simulations (Carrick et al. 2015; Boruah et al. 2020; Said et al. 2020). However, σ_v depends not only on the reconstruction method but also on the peculiar velocity sample. For this reason, we instead treat σ_v as a free parameter of the model with a Jeffreys prior $\pi(\sigma_v) \propto 1/\sigma_v$. As shown in Fig. 5 and Fig. 6, the inferred σ_v correlates inversely with the goodness-of-fit and hence σ_v provides a good indicator of the quality of a reconstruction. However, because of the dependence of σ_v on the sample in question, it should not be compared between samples, but only between reconstructions for a given sample. For example, a galaxy catalogue with primarily field galaxies will have a lower σ_v than a catalogue with galaxies in clusters because of the greater small-scale motions (not captured by the reconstructions) in the latter.

We then examined the parameter β , which scales the predicted velocity field. For C15, we denote it as β^* which is related to the growth rate of structure (see Section 4.6). For the other reconstructions, where velocities are consistently sourced by total matter distribution (except L24), scaling the predicted velocity field with β should not be necessary, implying $\beta = 1$. However, even in these cases, if allowed to vary the recovered β can be affected by the resolution at which the field is constrained, inaccurate reconstruction or discrepancies between the cosmological parameters assumed by the reconstruction and the actual parameters of the Universe. For example, an overly smoothed field may exhibit suppressed velocities, necessitating $\beta > 1$. We tested this hypothesis in Fig. 7 by treating β as a free parameter for all reconstructions. We find that CSiBORG2 is consistent with $\beta = 1$ for most samples, except for the SFI++ and CF4 TFR *i*-band samples, where it shows a higher bias. Interestingly, both S18 and C23 require higher values of β on these catalogues as well. On the other hand, L24 prefers a lower β value, indicating that the machine learning model may have overpredicted the velocities.

Regarding the external flow magnitude, it is noteworthy that L24 indicate their neural network reconstruction is sensitive to “super-survey” scales through redshift-space distortions. Our findings in Fig. 8 support this claim, as the external flow magnitude required by L24 is nearly consistent with zero, a distinction not seen in other reconstructions which also use the same redshift-space data. The preferred model, CSiBORG2, also favours a relatively small external flow, whereas the less favoured CSiBORG1 requires a substantially larger flow magnitude. However, similar to β , there is no clear relationship between the goodness-of-fit and the external flow magnitude.

Lastly, we analysed the predicted bulk flow curves by combining the internal bulk flow of each reconstruction with the external flow. Near the origin, our position provides a constraint on the bulk flow through the LG-CMB velocity, as derived from the CMB dipole (Planck Collaboration et al. 2020a). As shown in Fig. 11, all reconstructions (with the

possible exception of **CSiBORG1**) are consistent with this velocity when accounting for σ_v , which reflects the expected scatter between a given galaxy’s velocity and the velocity field estimate at its position.

Regarding the radial dependence, we find that while each reconstruction tracks a somewhat distinct bulk flow curve, there is a general agreement in the bulk flow direction at radii of approximately $100h^{-1}$ Mpc among **C15**, **L24**, **S18**, and **C23**. The **BORG** reconstructions, however, exhibit bulk flows that point in different directions, with **CSiBORG2** aligning more closely with those mentioned but slightly shifted towards the Shapley Supercluster (approximately $\ell = 305^\circ$, $b = 32^\circ$). Interestingly, **S18** calibrated against the 2MTF and CF4 TFR i -band samples also points in this direction. Since our peculiar velocity samples are generally limited to redshifts below $z = 0.05$, we do not draw comparisons with [Watkins et al. \(2023\)](#), who report unexpectedly large and increasing bulk flows at radii of $150 - 250h^{-1}$ Mpc.

5.2 Interpretation of results

While we have determined the relative preferences for the local Universe reconstructions, the reasons underlying these preferences remain unclear. To address this, we extend our analysis in two ways. First, we divide the galaxy samples into subsets based on their observed redshift, inclination errors, or absolute magnitude, and repeat the evidence comparison for each subset. Second, we correlate differences in log-likelihoods between reconstructions with galaxy properties in an attempt to discover which types of galaxy drive the preference or some reconstructions over others.

We begin by considering tracers with observed redshift $z_{\text{CMB}} < 0.025$ to examine the inner regions of the reconstructions, compared to the usual threshold of $z_{\text{CMB}} < 0.05$. The evidence ratios for all peculiar velocity samples remain qualitatively identical to those presented in Fig. 4: **CSiBORG2** is the most preferred reconstruction, **C15** and **L24** exhibit the second- and third-best goodness-of-fit, respectively, with similar performance, while the CosmicFlows reconstructions are disfavoured. Next, we focus only on the CF4 TFR i - and $W1$ -band samples, dividing them into subsets of galaxies with either below- or above-average inclination errors, and analyse the evidence ratios in both cases. As before, the conclusions from our fiducial analysis are robust to these variations. Since inclination errors propagate into the linewidth measurements and are already accounted for, this outcome is unsurprising. It does however indicate that there are not systematic errors associated with the linewidth that scale with the observational uncertainties. Lastly, we estimate the absolute magnitude of each galaxy from its apparent magnitude and redshift-space distance (converting the observed redshift in the CMB frame into a distance modulus). The two CF4 TFR samples are then split into subsets of the 25% brightest and faintest galaxies, and the evidence ratios are recomputed. Yet again, we find that our qualitative conclusions are unchanged.

Next, we repeat our fiducial analysis on the CF4 TFR sample without splitting the data and including the inhomogeneous Malmquist bias term. We record the log-likelihood of each galaxy at each posterior sample and compute the average likelihood $\langle L \rangle$. Subsequently, we calculate the differences in $\log\langle L \rangle$ between reconstructions on the same pe-

culiar velocity samples and correlate these differences with galaxy properties: sky position, observed redshift, apparent magnitude, linewidth, linewidth error, inclination, and inclination error.

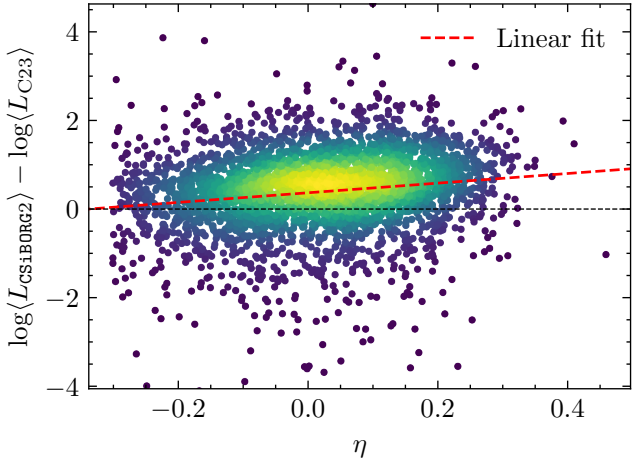
Among these features, significant trends emerge only for linewidth and observed redshift. The most pronounced differences occur when comparing **CSiBORG2** with **C23**. In Fig. 15a, we show a scatter plot of the differences in $\log\langle L \rangle$ between **CSiBORG2** and **C23** as a function of linewidth in the CF4 TFR $W1$ -band sample. We find a Spearman correlation coefficient of 0.18 (p -value of 10^{-27}), indicating that **CSiBORG2** is favoured more for galaxies with larger linewidths, corresponding to more massive objects. Since these trace higher-density regions, this result reaffirms that the improved performance of **CSiBORG2** is partly due to its better non-linear modelling via **BORG**. Similar significant trends are observed when comparing **CSiBORG2** with all other reconstructions, including **CSiBORG1**.

Fig. 15b illustrates that **CSiBORG2** consistently achieves higher likelihoods for galaxies at greater distances when compared to the least effective reconstructions **C23** (Spearman correlation coefficient of 0.23, p -value of 10^{-42}) or **S18**. This suggests that the constraints from CosmicFlows-based reconstructions degrade more rapidly with distance, despite the reconstructed volume in **C23** extending up to $z = 0.08$. However, even though **CSiBORG2** demonstrates better performance for brighter and more distant galaxies, we have confirmed that its preference remains significant even when considering only nearby or faint objects. The trend with observed redshift is not found for either **C15** or **L24** when compared to **CSiBORG2**. Interestingly, there is no preference between **CSiBORG2** and **C23** for the nearest or lowest-linewidth galaxies.

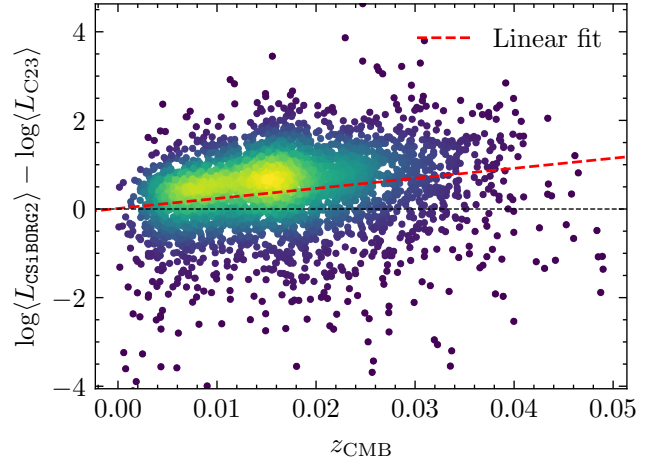
5.3 Caveats

One caveat in our comparison is that the goodness-of-fit depends on the resolution of the reconstruction. Higher resolution reconstructions would be expected to be preferred simply because they can capture smaller scale motions (before they become noise-dominated). To test this, we smoothed all fields to the same, coarse resolution shown in Fig. 4, which did not change our main conclusions: CosmicFlows-based reconstructions remain disfavoured, though **C15** becomes preferred over **CSiBORG2**. However, reaching higher resolutions is an advantage of a reconstruction method as, in principle, the goal is to reconstruct the local Universe down to non-linear scales, reducing the required extra random scatter σ_v . The preference of the 2M++-derived reconstructions over CosmicFlows-derived ones suggests either that the former dataset is more informative, or that there are limitations of the methods applied to the CosmicFlows data. On one hand, this result is surprising as the peculiar velocities probe directly the matter distribution of the Universe, whereas working with galaxy fields requires a careful bias treatment. On the other hand, while the 2M++ galaxy redshift-space positions are in practice nearly only shot-noise dominated, the CosmicFlows peculiar velocity data is noisy and sparse: out of the 38,000 objects in the grouped CF4 catalogue used by **C23** only 18,000 are within $z_{\text{CMB}} < 0.05$.

We attempt a broad comparison of the reconstructions available in the literature, without separating the ef-



(a) The difference in $\log\langle L\rangle$ as a function of linewidth η . The Spearman correlation coefficient is 0.18 (p -value of 10^{-27}).



(b) The difference in $\log\langle L\rangle$ as a function of observed redshift z_{CMB} . The Spearman correlation coefficient is 0.23 (p -value of 10^{-42}).

Figure 15. Differences in the logarithms of the average likelihoods of individual galaxies $\log\langle L\rangle$, averaged over the posterior samples, between **CSiBORG2** and the reconstruction by **Courtois et al. (2023)**. The plots illustrate these differences as functions of linewidth η (left) and observed redshift z_{CMB} (right). Positive values indicate preference for **CSiBORG2** and we include a line of best fit. This indicates that that **CSiBORG2** is preferentially better than the field of **Courtois et al. (2023)** for higher linewidth (mass) galaxies and at higher redshifts. No significant trends are found with other galaxy properties.

fect of the reconstruction technique and the input data. For instance, **S18** is based on a grouped version of the CF2 catalogue, which contains only $\sim 5,000$ galaxies. In contrast, **C23**, another reconstruction based on peculiar velocities, uses the larger CF4 catalogue, yet performs similarly to **S18** according to our metrics. We demonstrated that the non-linear **BORG**-based reconstructions outperform the other methods. However, this improvement does come at a significantly higher computational cost to obtain the ICs. Once the **BORG**-based reconstructions are produced, though, this computational cost is irrelevant for any follow-up analysis. In this respect it is worth noting that reconstruction of the velocity field is not a main aim of the **BORG** programme, but rather it comes “for free.” Nevertheless, it is worth emphasising that the linear method of **C15**, while orders of magnitude less computationally expensive than **BORG**, still performs better than both **S18** and **C23**.

We do not evaluate the quality of the reconstructions in specific regions but instead use all-sky samples. The TFR samples mainly include disk (field) galaxies, leading to a focus on lower-density regions rather than galaxy clusters. Evaluating velocities in clusters, which could be done with a fundamental plane sample, is beyond our present scope. However, we discovered in Section 5.2 that the preference for **BORG** is even greater for brighter galaxies. Since these trace on average higher density regions, it is likely that the fundamental plane would provide even greater evidence for **BORG**. An example of related work is that by **Sorce et al. (2024)** who examined velocities along the LOS to nearby clusters.

5.4 Comparison with literature

Peculiar velocity corrections are essential for any local Universe cosmology to model deviations from the Hubble

flow. For instance, in the main Pantheon+ supernova analysis (**Brout et al. 2022**), **Carr et al. (2022)** define “Hubble diagram redshifts,” z_{HD} , which are derived by converting the observed heliocentric supernova (host) redshifts to the CMB frame and applying corrections for peculiar motion based on **C15**.

The selection of **C15** was previously motivated by **Peterson et al. (2022)**, who found it to be the most effective in reducing scatter in the supernova Hubble diagram. Although the only common reconstruction between **Peterson et al. (2022)** and this work is **C15**, their analysis also included a CosmicFlows3-based reconstruction (**Tully et al. 2016**), which was found to increase the scatter rather than reduce it. This conclusion aligns qualitatively with our findings, where we identify the reconstruction by **C15** as preferred over the CosmicFlows-based reconstructions. However, we also demonstrate that the latest **BORG** reconstruction has the potential to reduce scatter in the Hubble diagram even further. Moreover, unlike **C15**, **BORG** provides a measure of reconstruction uncertainty, allowing for propagation of this uncertainty into the resulting Hubble diagram.

A related study is that of **Boruah et al. (2021)**, who compared **C15** to kernel-smoothed velocity field estimates derived from either fundamental plane or TFR samples by calculating a Bayesian model evidence. They show that the kernel-smoothed velocity estimates are disfavoured when compared to independent peculiar velocity samples.

5.5 Future work

An evident extension of our work is the inclusion of additional peculiar velocity tracers. Two promising candidates are larger supernova samples and fundamental plane galaxy samples. The primary advantage of supernova samples lies in their smaller distance errors, approximately $\sim 5\%$, com-

pared to the $\sim 20\%$ TFR errors. However, supernova samples are generally smaller in size.

One major supernova dataset is Pantheon+ (Brout et al. 2022), which combines several low-redshift supernova surveys. We excluded this sample from our analysis because it would require careful systematic treatment of the constituent surveys, relying on the covariance matrix provided by Brout et al. (2022). However, this matrix already includes peculiar velocity corrections based on C15, and disentangling these corrections is non-trivial. Simply subtracting their contributions results in a singular, non-invertible covariance matrix (that parts of the Pantheon+ covariance matrix are not positive semi-definite was already noted by Lane et al. 2024). Another promising supernova dataset is the Zwicky Transient Facility (ZTF) SN Ia DR2, a volume-limited, unbiased sample of 1000 supernovae below $z_{\text{CMB}} \sim 0.06$ (Amenouche et al. 2024). However, this dataset is not yet publicly available. Two relevant fundamental plane samples are those from the 6dF Galaxy Survey (Campbell et al. 2014) and SDSS (Howlett et al. 2022). Both have been utilised by Said et al. (2020) to calibrate the field of C15, albeit their approach relied on forward modelling the galaxy angular size rather than galaxy distance as we do here. Nevertheless, the consistent evidence comparison across all supernova and TFR samples used in this work indicates that our results are robust to choice of dataset, and hence similar conclusions would likely be reached using Pantheon+ or ZTF DR2.

6 CONCLUSION

We introduce a novel framework for jointly calibrating distance indicator relations and velocity field reconstructions using peculiar velocity data in the local Universe. Unlike previous studies, we carefully account for uncertainties in distance-indicating properties within a Bayesian hierarchical model. We use reconstructions summarised in Table 1 that include linear theory (Carrick et al. 2015; Sorce 2018), machine learning (Lilow et al. 2024), and resimulations of density field constraints derived from Bayesian forward modelling of either redshift-space galaxy positions (BORG; Jasche & Lavaux 2019; Stopyra et al. 2024) or peculiar velocities (Courtois et al. 2023). We apply this framework to TFR and supernova samples summarised in Table 2, with future plans to extend it to fundamental plane samples. Under a weak assumption we compute the Bayesian model evidence for the joint distance and flow calibration described in Section 3.2, enabling us to compare how well different local Universe reconstructions explain the available peculiar velocity data.

We show that while by our metrics the older BORG reconstruction did not outperform the linear reconstruction of Carrick et al. (2015), the more recent and improved BORG reconstruction based on ICs of Stopyra et al. (2024) is significantly preferred. This suggests a strong future potential for non-linear modelling within the BORG framework. We also evaluated the neural-network-based reconstruction of Lilow et al. (2024), however, we found that it performs similarly to Carrick et al. (2015), and even marginally worse in some cases. Finally, the CosmicFlows-based reconstructions by Sorce (2018) and Courtois et al. (2023) were disfavoured.

We further established that σ_v , the scatter between predicted and observed redshifts, serves as a reliable indicator of the ability of a reconstruction to make the data. Moreover β , the velocity field scaling parameter, is generally consistent with 1 for the preferred CSiBORG2 reconstruction, except in the SFI++ and CF4 TFR *i*-band samples, where it is over-predicted. This suggests that the velocities need to be scaled up to match observations, which is interestingly also true of the two CosmicFlows-based reconstructions.

We also studied the predicted LG motion in the CMB frame. Due to the σ_v scatter, we found that all reconstructions are broadly consistent with the CMB-derived LG velocity (Planck Collaboration et al. 2020a). We also compared the predicted bulk flow curves as a function of radius and found similar qualitative trends, though the quantitative details vary.

Finally, we calibrated the β^* velocity scaling of the linear theory reconstruction of Carrick et al. (2015) using our peculiar velocity samples, enabling us to place a stringent constraint on the parameter $S_8 \equiv \sigma_8 \sqrt{\Omega_m/0.3}$. For the joint sample, we determined $\beta^* = 0.392 \pm 0.0146$, which translates to $S_8 = 0.69 \pm 0.034$. This estimate of S_8 agrees with other peculiar velocity-based measurements but exhibits a $\sim 2\sigma$ tension with weak lensing constraints and a 4.1σ tension with Planck, thus exacerbating the S_8 tension.

In conclusion, this work provides a comprehensive comparison of various velocity field reconstructions available in the literature, identifying the latest BORG reconstruction based on ICs from Stopyra et al. (2024) as the most strongly preferred. We anticipate that this framework and our results will be valuable not only for evaluating local Universe reconstructions but also for cosmological analyses that rely on peculiar velocity corrections, such as supernovae or the dark siren method for gravitational waves. This is particularly relevant in the context of the current Hubble tension and, more broadly, for any inference requiring physical distances to galaxies.

7 DATA AVAILABILITY

The code underlying this article is available at <https://github.com/Richard-Sti/csiborgtools>. The Carrick et al. (2015) reconstruction is available at <https://cosmicflows.iap.fr>, the Lilow et al. (2024) reconstruction at <https://github.com/rilow/2MRS-NeuralNet> and the Courtois et al. (2023) reconstruction at <https://projets.ip2i.in2p3.fr/cosmicflows/>. The public CF4 data is available at <https://edd.ifa.hawaii.edu/dfirst.php>. All other data will be made available on reasonable request to the authors.

ACKNOWLEDGEMENTS

We thank Indranil Banik, Supranta S. Boruah, Pedro G. Ferreira, Sebastian von Hausegger, Wojciech Hellwing, Amber Hollinger, Jens Jasche, Ehsan Kourkchi, Sergij Mazurenko, Stuart McAlpine, Alicja Polanska, Jenny Sorce, Stephen Stopyra and Tariq Yasin for useful inputs and discussions. We also thank Jonathan Patterson for smoothly running the Glamdring Cluster hosted by the University of Oxford,

where the data processing was performed. This work was done within the Aquila Consortium⁸.

RS acknowledges financial support from STFC Grant No. ST/X508664/1, the Snell Exhibition of Balliol College, Oxford, and the CCA Pre-doctoral Program. HD is supported by a Royal Society University Research Fellowship (grant no. 211046). DJB is supported by the Simons Collaboration on “Learning the Universe.” This project has received funding from the European Research Council (ERC) under the European Union’s Horizon 2020 research and innovation programme (grant agreement No 693024). This work was performed using the DiRAC Data Intensive service at Leicester, operated by the University of Leicester IT Services, which forms part of the STFC DiRAC HPC Facility (www.dirac.ac.uk). The equipment was funded by BEIS capital funding via STFC capital grants ST/K000373/1 and ST/R002363/1 and STFC DiRAC Operations grant ST/R001014/1. DiRAC is part of the National e-Infrastructure. For the purpose of open access, we have applied a Creative Commons Attribution (CC BY) licence to any Author Accepted Manuscript version arising.

REFERENCES

- Abazajian K. N., et al., 2009, *ApJS*, **182**, 543
- Abbott B. P., et al., 2018, *Living Reviews in Relativity*, **21**, 3
- Abbott T. M. C., et al., 2020, *Phys. Rev. D*, **102**, 023509
- Abbott B. P., et al., 2021, *ApJ*, **909**, 218
- Abbott T. M. C., et al., 2022, *Phys. Rev. D*, **105**, 023520
- Adams C., Blake C., 2017, *MNRAS*, **471**, 839
- Adams C., Blake C., 2020, *MNRAS*, **494**, 3275
- Amenouche M., et al., 2024, *arXiv e-prints*, p. [arXiv:2409.04650](https://arxiv.org/abs/2409.04650)
- Amon A., et al., 2022, *Phys. Rev. D*, **105**, 023514
- Astropy Collaboration et al., 2013, *A&A*, **558**, A33
- Astropy Collaboration et al., 2018, *AJ*, **156**, 123
- Astropy Collaboration et al., 2022, *ApJ*, **935**, 167
- Bartlett D. J., Desmond H., 2023, *The Open Journal of Astrophysics*, **6**, 42
- Bartlett D. J., Desmond H., Ferreira P. G., 2021, *Phys. Rev. D*, **103**, 023523
- Bartlett D. J., Kostić A., Desmond H., Jasche J., Lavaux G., 2022, *Phys. Rev. D*, **106**, 103526
- Bartlett D. J., Wandelt B. D., Zennaro M., Ferreira P. G., Desmond H., 2024, *A&A*, **686**, A150
- Bocquet S., et al., 2019, *ApJ*, **878**, 55
- Boruah S. S., Hudson M. J., Lavaux G., 2020, *MNRAS*, **498**, 2703
- Boruah S. S., Hudson M. J., Lavaux G., 2021, *MNRAS*, **507**, 2697
- Boubel P., Colless M., Said K., Staveley-Smith L., 2024a, *MNRAS*, **531**, 84
- Boubel P., Colless M., Said K., Staveley-Smith L., 2024b, *MNRAS*, **533**, 1550
- Bouchet F. R., Colombi S., Hivon E., Juszkiewicz R., 1995, *A&A*, **296**, 575
- Boyd B. M., Grayling M., Thorp S., Mandel K. S., 2024, *arXiv e-prints*, p. [arXiv:2407.15923](https://arxiv.org/abs/2407.15923)
- Brout D., et al., 2022, *ApJ*, **938**, 110
- Calabrese E., Slosar A., Melchiorri A., Smoot G. F., Zahn O., 2008, *Phys. Rev. D*, **77**, 123531
- Campbell L. A., et al., 2014, *MNRAS*, **443**, 1231
- Carr A., Davis T. M., Scolnic D., Said K., Brout D., Peterson E. R., Kessler R., 2022, *Publ. Astron. Soc. Australia*, **39**, e046
- Carrick J., Turnbull S. J., Lavaux G., Hudson M. J., 2015, *MNRAS*, **450**, 317
- Colombi S., Chodorowski M. J., Teyssier R., 2007, *MNRAS*, **375**, 348
- Conlin R., 2024, *quadx*, doi:10.5281/zenodo.12823258, <https://doi.org/10.5281/zenodo.12823258>
- Courtois H. M., Dupuy A., Guinet D., Baulieu G., Ruppin F., Brenas P., 2023, *A&A*, **670**, L15
- DESI Collaboration et al., 2024, *arXiv e-prints*, p. [arXiv:2411.12022](https://arxiv.org/abs/2411.12022)
- Dálya G., et al., 2022, *MNRAS*, **514**, 1403
- Dark Energy Survey and Kilo-Degree Survey Collaboration et al., 2023, *The Open Journal of Astrophysics*, **6**, 36
- Davis T. M., et al., 2011, *ApJ*, **741**, 67
- Dupuy A., Courtois H. M., Kubik B., 2019, *MNRAS*, **486**, 440
- Dvali G., Gabadadze G., Porrati M., 2000, *Physics Letters B*, **485**, 208
- Efstathiou G., Kaiser N., Saunders W., Lawrence A., Rowan-Robinson M., Ellis R. S., Frenk C. S., 1990, *MNRAS*, **247**, 10P
- Feix M., Branchini E., Nusser A., 2017, *MNRAS*, **468**, 1420
- Feldman H. A., Watkins R., Hudson M. J., 2010, *MNRAS*, **407**, 2328
- Foley R. J., et al., 2018, *MNRAS*, **475**, 193
- Ganeshalingam M., Li W., Filippenko A. V., 2013, *MNRAS*, **433**, 2240
- Gelman A., Rubin D. B., 1992, *Statistical Science*, **7**, 457
- Graziani R., Courtois H. M., Lavaux G., Hoffman Y., Tully R. B., Copin Y., Pomarède D., 2019, *MNRAS*, **488**, 5438
- Guy J., et al., 2007, *A&A*, **466**, 11
- Hellwing W. A., Bilicki M., Libeskind N. I., 2018, *Phys. Rev. D*, **97**, 103519
- Heymans C., et al., 2021, *A&A*, **646**, A140
- Hinshaw G., et al., 2009, *ApJS*, **180**, 225
- Hoffman M. D., Gelman A., 2011, *arXiv e-prints*, p. [arXiv:1111.4246](https://arxiv.org/abs/1111.4246)
- Hoffman Y., Courtois H. M., Tully R. B., 2015, *MNRAS*, **449**, 4494
- Hogg D. W., 1999, *arXiv e-prints*, pp astro-ph/9905116
- Hollinger A. M., Hudson M. J., 2024, *MNRAS*, **531**, 788
- Hong T., et al., 2019, *MNRAS*, **487**, 2061
- Howlett C., Said K., Lucey J. R., Colless M., Qin F., Lai Y., Tully R. B., Davis T. M., 2022, *MNRAS*, **515**, 953
- Hubble E. P., 1926, *ApJ*, **64**, 321
- Huchra J. P., et al., 2012, *ApJS*, **199**, 26
- Huterer D., Shafer D. L., Scolnic D. M., Schmidt F., 2017, *J. Cosmology Astropart. Phys.*, **2017**, 015
- Jasche J., Lavaux G., 2019, *A&A*, **625**, A64
- Jasche J., Wandelt B. D., 2013, *MNRAS*, **432**, 894
- Jones D. H., et al., 2009, *MNRAS*, **399**, 683
- Jones D. O., et al., 2019, *ApJ*, **881**, 19
- Juszkiewicz R., Feldman H. A., Fry J. N., Jaffe A. H., 2010, *J. Cosmology Astropart. Phys.*, **2010**, 021
- Kourkchi E., Tully R. B., Neill J. D., Seibert M., Courtois H. M., Dupuy A., 2019, *ApJ*, **884**, 82
- Kourkchi E., Tully R. B., Anand G. S., Courtois H. M., Dupuy A., Neill J. D., Rizzi L., Seibert M., 2020a, *ApJ*, **896**, 3
- Kourkchi E., et al., 2020b, *ApJ*, **902**, 145
- Lane Z. G., Seifert A., Ridden-Harper R., Wiltshire D. L., 2024, *MNRAS*,
- Lavaux G., Hudson M. J., 2011, *MNRAS*, **416**, 2840
- Lavaux G., Jasche J., 2016, *MNRAS*, **455**, 3169
- Lavaux G., Jasche J., Leclercq F., 2019, *arXiv e-prints*, p. [arXiv:1909.06396](https://arxiv.org/abs/1909.06396)
- Li W. D., et al., 2000, in Holt S. S., Zhang W. W., eds, *American Institute of Physics Conference Series Vol. 522, Cosmic Explosions: Tenth AstroPhysics Conference*. AIP, pp 103–106 ([arXiv:astro-ph/9912336](https://arxiv.org/abs/astro-ph/9912336)), doi:10.1063/1.1291702

⁸ <https://aquila-consortium.org>

Lilou R., Ganeshiah Veena P., Nusser A., 2024, [arXiv e-prints](#), p. [arXiv:2404.02278](#)
 Linder E. V., Cahn R. N., 2007, *Astroparticle Physics*, **28**, 481
 Madhavacheril M. S., et al., 2024, *ApJ*, **962**, 113
 March M. C., Trotta R., Berkes P., Starkman G. D., Vaudrevange P. M., 2011, *MNRAS*, **418**, 2308
 March M. C., Karpenka N. V., Feroz F., Hobson M. P., 2014, *MNRAS*, **437**, 3298
 March M. C., Wolf R. C., Sako m., D’Andrea C., Brout D., 2018, [arXiv e-prints](#), p. [arXiv:1804.02474](#)
 Masters K. L., Springob C. M., Haynes M. P., Giovanelli R., 2006, *ApJ*, **653**, 861
 Masters K. L., Springob C. M., Huchra J. P., 2008, *AJ*, **135**, 1738
 McEwen J. D., Wallis C. G. R., Price M. A., Spurio Mancini A., 2021, [arXiv e-prints](#), p. [arXiv:2111.12720](#)
 Mead A. J., Heymans C., Lombriser L., Peacock J. A., Steele O. I., Winther H. A., 2016, *MNRAS*, **459**, 1468
 Monaghan J. J., 1992, *ARA&A*, **30**, 543
 Nusser A., 2016, *MNRAS*, **455**, 178
 Nusser A., 2017, *MNRAS*, **470**, 445
 Nusser A., Davis M., 2011, *ApJ*, **736**, 93
 Peery S., Watkins R., Feldman H. A., 2018, *MNRAS*, **481**, 1368
 Peterson E. R., et al., 2022, *ApJ*, **938**, 112
 Phan D., Pradhan N., Jankowiak M., 2019, [arXiv e-prints](#), p. [arXiv:1912.11554](#)
 Pike R. W., Hudson M. J., 2005, *ApJ*, **635**, 11
 Planck Collaboration et al., 2014, *A&A*, **571**, A1
 Planck Collaboration et al., 2016, *A&A*, **594**, A24
 Planck Collaboration et al., 2020a, *A&A*, **641**, A1
 Planck Collaboration et al., 2020b, *A&A*, **641**, A6
 Polanska A., Price M. A., Piras D., Spurio Mancini A., McEwen J. D., 2024, [arXiv e-prints](#), p. [arXiv:2405.05969](#)
 Porqueres N., Kodi Ramanah D., Jasche J., Lavaux G., 2019, *A&A*, **624**, A115
 Porredon A., et al., 2022, *Phys. Rev. D*, **106**, 103530
 Riess A. G., et al., 2011, *ApJ*, **730**, 119
 Riess A. G., et al., 2022, *ApJ*, **934**, L7
 Rubin D., et al., 2015, *ApJ*, **813**, 137
 Rubin D., et al., 2023, [arXiv e-prints](#), p. [arXiv:2311.12098](#)
 Said K., Colless M., Magoulas C., Lucey J. R., Hudson M. J., 2020, *MNRAS*, **497**, 1275
 Scrimgeour M. I., et al., 2016, *MNRAS*, **455**, 386
 Skilling J., 2006, *Bayesian Analysis*, **1**, 833
 Skrutskie M. F., et al., 2006, *AJ*, **131**, 1163
 Smith R. E., et al., 2003, *MNRAS*, **341**, 1311
 Sorce J. G., 2018, *MNRAS*, **478**, 5199
 Sorce J. G., 2020, *MNRAS*, **495**, 4463
 Sorce J. G., Mohayaee R., Aghanim N., Dolag K., Malavasi N., 2024, *A&A*, **687**, A85
 Springel V., 2005, *MNRAS*, **364**, 1105
 Springel V., Pakmor R., Zier O., Reinecke M., 2021, *MNRAS*, **506**, 2871
 Springob C. M., Masters K. L., Haynes M. P., Giovanelli R., Marinoni C., 2007, *ApJS*, **172**, 599
 Srinivasan R., Crisostomi M., Trotta R., Barausse E., Breschi M., 2024, [arXiv e-prints](#), p. [arXiv:2404.12294](#)
 Stopyra S., Peiris H. V., Pontzen A., Jasche J., Lavaux G., 2024, *MNRAS*, **527**, 1244
 Strauss M. A., Willick J. A., 1995, *Phys. Rep.*, **261**, 271
 Sui C., Bartlett D. J., Pandey S., Desmond H., Ferreira P. G., Wandelt B. D., 2024, [arXiv e-prints](#), p. [arXiv:2410.14623](#)
 Takahashi R., Sato M., Nishimichi T., Taruya A., Oguri M., 2012, *ApJ*, **761**, 152
 Tassev S., Zaldarriaga M., Eisenstein D. J., 2013, *J. Cosmology Astropart. Phys.*, **2013**, 036
 Teyssier R., 2002, *A&A*, **385**, 357
 Tripp R., 1998, *A&A*, **331**, 815
 Tully R. B., Fisher J. R., 1977, *A&A*, **54**, 661

Tully R. B., et al., 2013, *AJ*, **146**, 86
 Tully R. B., Courtois H. M., Sorce J. G., 2016, *AJ*, **152**, 50
 Tully R. B., et al., 2023, *ApJ*, **944**, 94
 Villaescusa-Navarro F., et al., 2020, *ApJS*, **250**, 2
 Virtanen P., et al., 2020, *Nature Methods*, **17**, 261
 Wang L., Steinhardt P. J., 1998, *ApJ*, **508**, 483
 Watkins R., Feldman H. A., 2015, *MNRAS*, **447**, 132
 Watkins R., Feldman H. A., Hudson M. J., 2009, *MNRAS*, **392**, 743
 Watkins R., et al., 2023, *MNRAS*, **524**, 1885
 Westover M., 2007, PhD thesis, Harvard University
 Whitford A. M., Howlett C., Davis T. M., 2023, *MNRAS*, **526**, 3051
 Yahil A., Strauss M. A., Davis M., Huchra J. P., 1991, *ApJ*, **372**, 380

APPENDIX A: SUPERNOVA FLOW MODEL

In Section 3.2, we derived the model for joint density and velocity field calibration $(\alpha, \beta, \sigma_v, \mathbf{V}_{\text{ext}})$, alongside the calibration of the TFR. We now extend this framework to supernova calibration, aiming to infer the Tripp parameters \mathcal{A} and \mathcal{B} , as well as the absolute magnitude of Type Ia supernovae, M_{SN} . For this purpose, we consider the “observed” SALT2 light curve parameters: stretch $x_{1,\text{obs}}$, colour correction c_{obs} , and apparent magnitude m_{obs} , along with their corresponding “true” values $x_{1,\text{true}}$, c_{true} , and m_{true} .

The primary difference compared to the TFR model is in the replacement of μ_{TFR} with the supernova distance estimate μ_{SN} , which is calculated from the true variables as

$$\mu_{\text{SN}} \equiv m_{\text{true}} + \mathcal{A}x_{1,\text{true}} - \mathcal{B}c_{\text{true}} - M_{\text{SN}}, \quad (\text{A1})$$

This enables sampling of the supernova distance as:

$$\begin{aligned}
 p(\mu_{\text{true}} | x_{1,\text{true}}, c_{\text{true}}, m_{\text{true}}, \boldsymbol{\theta}) &= \\
 &= \frac{r^2(\mu_{\text{true}})n(\mu_{\text{true}})}{\mathcal{C}(\boldsymbol{\theta})} \frac{dr}{d\mu} \Big|_{\mu_{\text{true}}} \mathcal{N}(\mu_{\text{true}}; \mu_{\text{SN}}, \sigma_{\text{SN}}).
 \end{aligned} \quad (\text{A2})$$

Here, as before, r^2 accounts for the homogeneous Malmquist bias, n represents the inhomogeneous Malmquist bias, $dr/d\mu$ is the coordinate transformation of the Malmquist bias term from comoving distance to distance modulus, and the Gaussian term relates the supernova distance estimate to the true distance.

As before, we include a likelihood for the observed parameters, analogous to Eq. (22), for m , x_1 , and c . The true parameters are sampled from a Gaussian hyperprior:

$$\pi(m_{\text{true}}, x_{1,\text{true}}, c_{\text{true}} | \boldsymbol{\theta}) = \mathcal{N}(m_{\text{true}}, x_{1,\text{true}}, c_{\text{true}} | \boldsymbol{\mu}_{\text{SN}}, \mathbf{C}_{\text{SN}}), \quad (\text{A3})$$

where $\boldsymbol{\mu}_{\text{SN}}$ is the hyperprior mean of m_{true} , $x_{1,\text{true}}$, and c_{true} , inferred using uniform priors. The 3×3 covariance matrix \mathbf{C}_{SN} has standard deviations σ_i , which are inferred with Jeffreys’ prior $\pi(\sigma_i) \propto 1/\sigma_i$, and correlation coefficients, which are assigned uniform priors ranging from -1 to 1 , though this choice for a 3-dimensional covariance matrix no longer guarantees a positive semi-definite matrix. However, we do not encounter this problem in our inference. Altogether, the

final likelihood is simply

$$\begin{aligned}
\mathcal{L}(z_{\text{CMB}}, m_{\text{obs}}, \eta_{\text{obs}} | \boldsymbol{\theta}, m_{\text{true}}, \eta_{\text{true}}) = & \\
& \int dr \mathcal{N}(cz_{\text{CMB}}; cz_{\text{pred}}, \sqrt{\sigma_v^2 + \sigma_{cz_{\text{CMB}}}^2}) \\
& \times \frac{r^2 n(r) \mathcal{N}(\mu_{\text{true}}; \mu_{\text{SN}}, \sigma_{\text{SN}})}{\int r'^2 n(r') \mathcal{N}(\mu'_{\text{true}}; \mu_{\text{SN}}, \sigma_{\text{SN}}) dr'} \\
& \times \frac{S(m_{\text{obs}}) \mathcal{N}(m_{\text{obs}}; m_{\text{true}}, \sigma_m)}{\int S(m'_{\text{obs}}) \mathcal{N}(m'_{\text{obs}}; m_{\text{true}}, \sigma_m) dm'_{\text{obs}}} \\
& \times \frac{S(x_{1,\text{obs}}) \mathcal{N}(x_{1,\text{obs}}; x_{1,\text{true}}, \sigma_{x_1})}{\int S(\eta'_{\text{obs}}) \mathcal{N}(x'_{1,\text{obs}}; x_{1,\text{true}}, \sigma_{x_1}) dx'_{1,\text{true}}} \\
& \times \frac{S(c_{\text{obs}}) \mathcal{N}(c_{\text{obs}}; c_{\text{true}}, \sigma_c)}{\int S(c'_{\text{obs}}) \mathcal{N}(c'_{\text{obs}}; c_{\text{true}}, \sigma_c) dc'_{\text{true}}}, \tag{A4}
\end{aligned}$$

where compared to the TFR, where the likelihood term involved only η_{obs} , we now include likelihood terms for both $x_{1,\text{true}}$ and c_{true} .

Firstly, the advantage of this framework is that any corrections to the Tripp formula can be straightforwardly implemented by modifying Eq. (A1) and introducing additional terms, which may depend on factors such as galaxy mass or environment. Secondly, selection effects can be modelled through an analogue of Eq. (22). In Eq. (A2), we implicitly assumed independence between supernovae by not including a covariance matrix, as the Tripp calibration is inferred jointly. Furthermore, we neglected any correlations between the parameters of the SALT2 light curve. However, their covariance could be accounted for by replacing the one-dimensional conditional distribution of the measured parameters, given the true SALT2 parameters. However, incorporating selection effects in this context would be non-trivial and may require a simulation-based approach (Boyd et al. 2024).

APPENDIX B: POSTERIOR APPROXIMATION

In Section 3.2, we introduced a novel flow model that accounts for observational uncertainties, intrinsic source population, and selection effects. However, this model has the drawback of introducing an additional two (three) latent variables per galaxy for a TFR (supernova) peculiar velocity sample. While sampling in such high-dimensional spaces is feasible with an HMC, calculating the evidence is likely infeasible. To address this, in Section 3.4 we presented an approximate model for use in evidence calculations where the “true” latent variables are fixed to their observed values, and the observational uncertainties are added in quadrature with the intrinsic uncertainties. This approach is implicitly followed by Boruah et al. (2020) and other earlier works. The rationale for this method is that, in the case of the TFR relation, observational uncertainties are generally subdominant to the intrinsic scatter.

Here, we directly compare the two methods to verify that the approximate method is reliable. Fig. B1 shows the posteriors from the two methods for the CF4 TFR *i*-band sample and the CB2 reconstruction. We find that the only parameters significantly affected by use of the approximate method are the TFR zero-point a_{TFR} and the power-law density bias α . The remaining parameters remain largely

unchanged. This observation holds true across other combinations of reconstructions and peculiar velocity samples: only the distance calibration or the density bias parameters may be significantly shifted, though the example of Fig. B1 is the most extreme one. The zero-point is not the primary focus of this work, although its shift would be of significant interest for inferring the Hubble constant when including an absolute calibration. Due to the high dimensionality of the posterior, it is not possible to directly assess how this approximation affects the evidence ratios. In principle, one could test this approximation using another: assuming a Gaussian posterior and applying the Laplace approximation. However, we do not pursue this here, as we implicitly assume that any error introduced in the approximated evidence is sufficiently smaller than the differences in logarithmic evidences between samples when tested against different reconstructions, which, for the employed CF4 samples, is $\gg 1$. Moreover, since this approach would introduce an additional approximation to validate the initial one, its conclusions would not be guaranteed to hold.

This paper has been typeset from a $\text{\TeX}/\text{\LaTeX}$ file prepared by the author.

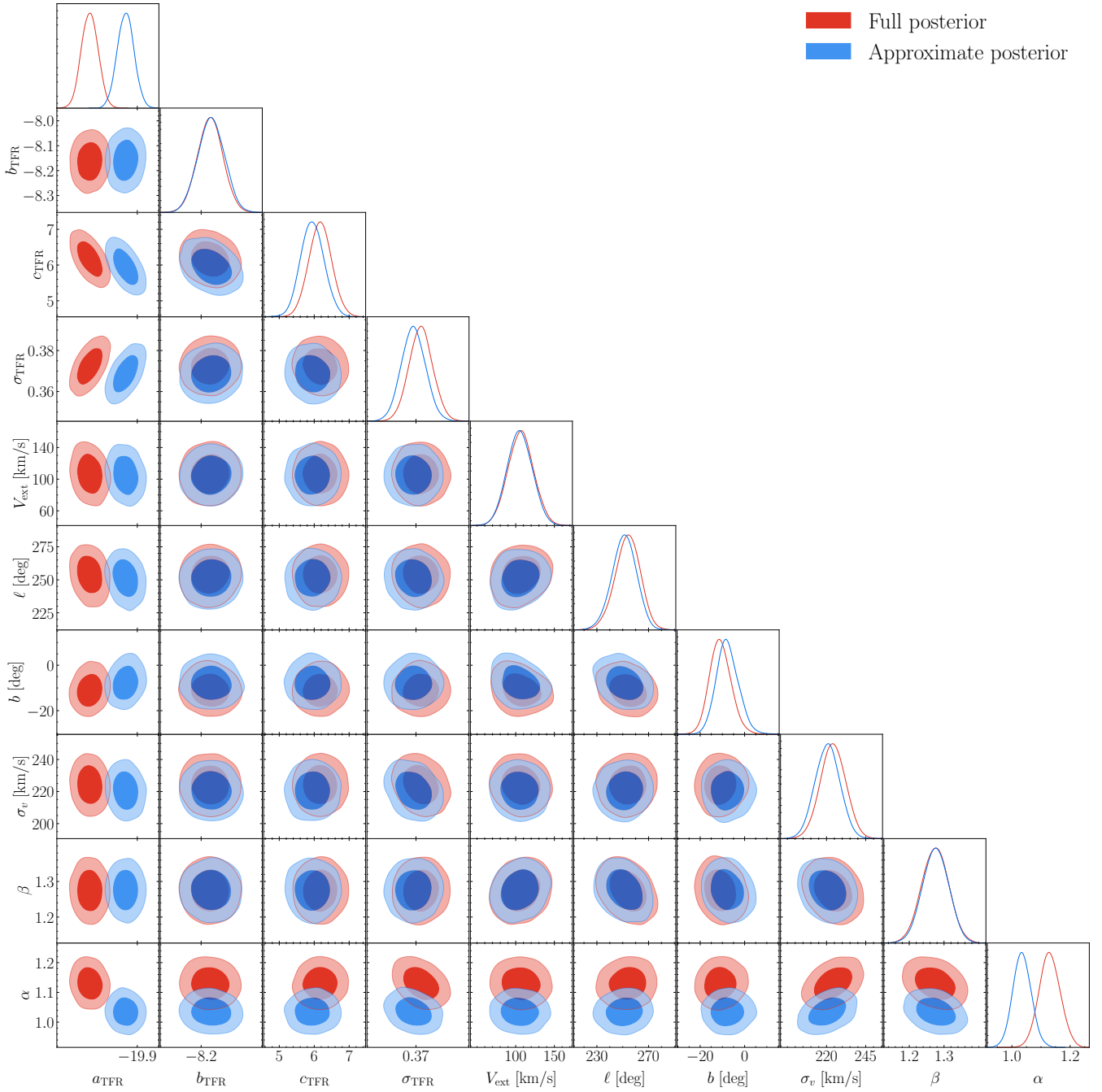


Figure B1. Example comparison of the inferred posteriors on the model parameters using the full likelihood from Eq. (23) (red) versus the approximate likelihood used for evidence calculation (Section 3.4; blue). The underlying reconstruction is CSiBORG2, and the peculiar velocity sample is the CF4 TFR i -band sample. Contours represent the 1σ and 2σ credible regions.